International Journal of Greenhouse Gas Control 75 (2018) 107–124

Contents lists available at ScienceDirect

International Journal of Greenhouse Gas Control

journal homepage: www.elsevier.com/locate/ijggc

Is CO_2 injection at Aquistore aseismic? A combined seismological and geomechanical study of early injection operations

A.L. Stork[a,*], C.G. Nixon[b], C.D. Hawkes[c], C. Birnie[d], D.J. White[e], D.R. Schmitt[b], B. Roberts[e]

[a] School of Earth Sciences, University of Bristol, Queens Rd, Bristol, BS8 1RJ, UK
[b] Department of Physics, University of Alberta, CCS 4-183, Edmonton, AB, T6G 2E1, Canada
[c] College of Engineering, University of Saskatchewan, 57 Campus Drive, Saskatoon, SK, S7N 5A9, Canada
[d] School of Earth and Environment, University of Leeds, Leeds, LS2 9JT, UK
[e] Geological Survey of Canada, 601 Booth St., Ottawa, ON, K1A 0E8, Canada

ARTICLE INFO

Keywords:
Carbon Capture and Storage (CCS)
Passive seismic monitoring
Geomechanics
Aquistore

ABSTRACT

Fluid injection is known to induce seismic events if the injection causes fracturing of the surrounding rock or if resulting pressure changes reactivate pre-existing faults and fractures. Carbon dioxide (CO_2) storage projects where CO_2 is injected into deep geological formations for permanent containment are one sector where induced seismicity has been observed. The Aquistore storage project in Saskatchewan, Canada began CO_2 injection into the basal Cambrian sandstone at ~3.2 km deep in April 2015 and the site has been extensively monitored for seismicity. Passive seismic monitoring instrumentation includes a small network of broadband seismometers, a continuously recording array of near-surface geophones and temporary deployments of downhole geophones at depths from 2950 m to 3010 m in an observation well. To date no injection-related induced seismicity has been observed. The seismic arrays are functioning as expected and local mine blasts, orientation shots and perforation shots have been detected using standard detection algorithms. Data stacking algorithms have also been tested on short-periods of data. Using synthetic data added to noise models, the estimated minimum detectable event local magnitude is −0.8 for the broadband stations and between −1.6 and −0.6 for the near-surface geophones. Thus far, small volumes of CO_2 have been injected at Aquistore (~140 kt) and injection has generally occurred below the fracture pressure. As a result, predicted pore pressure changes are small and periods without injection have allowed relaxation of the pressure plume. Geomechanical modelling suggests insignificant effective stress changes at an identified fault near the Aquistore injection well. It is therefore not surprising that no induced seismicity has been detected. With further injection, continued seismic monitoring is essential to provide warning of any fault reactivation and thus any potential increase in seismic risk or CO_2 leakage risk.

1. Introduction

Geological storage of carbon dioxide (CO_2) is one method proposed to reduce anthropogenic emission of the greenhouse gas to mitigate against climate change. Large-scale deployment of the technology will require not only the use of depleted hydrocarbon reservoirs, but also porous saline formations (e.g., IEAGHG, 2014). Successful commercial scale projects have been/are operating with injection into depleted oil and gas reservoirs for up to 20 years, for example at the Sleipner field offshore Norway (Chadwick and Noy, 2015); the Weyburn field in Saskatchewan, Canada (Wilson and Monea, 2004); and the In Salah field in Algeria (Ringrose et al., 2013). In 2015, two projects began injection into deep saline aquifers in Canada, at the Shell Quest project in Alberta (Tucker et al., 2016) and the Aquistore project in Saskatchewan (Worth et al., 2014).

CO_2 for geological storage is supplied to the Aquistore site from the adjacent coal-burning SaskPower Boundary Dam power plant. In 2014, CO_2 capture began at the plant at a rate of approximately 2400 t/day (White et al., 2016) and injection into Cambro-Ordovician sandstones overlying Precambrian basement rocks began in April 2015. Up to March 2018–140 kt of CO_2 has been injected at the Aquistore site with most of the captured CO_2 transported via pipeline to the Weyburn oil field for enhanced oil recovery operations. Results from time-lapse 3D seismic surveys (surface and VSP) in February 2016 show an area of CO_2 saturation in the injection formation, the upper Deadwood formation (Roach et al., 2017; White et al., 2017), extending at least 150 m north-west of the injection well.

At the Aquistore site, CO_2 is injected through casing perforations at

* Corresponding author.
E-mail address: anna.stork@bristol.ac.uk (A.L. Stork).

https://doi.org/10.1016/j.ijggc.2018.05.016
Received 1 October 2017; Received in revised form 30 April 2018; Accepted 18 May 2018

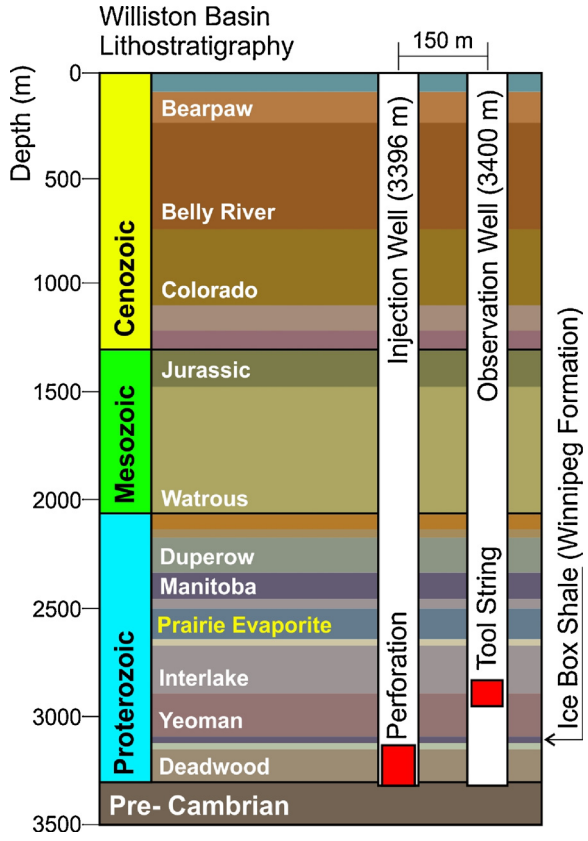

Fig. 1. Generalized stratigraphy at the Aquistore site. Depth ranges containing CO_2 injection perforations and the downhole geophone tool string in the two boreholes are shown in red.

depths of 3150–3350 m below the surface via one injection well. Deep fluid injection has the potential to induce seismicity. For example, McGarr et al. (2002) summarize several case histories where deep injection has resulted in felt events. Recently, other projects injecting CO_2 into basal Cambrian sandstones have seen associated small magnitude induced seismicity, termed *microseismicity*, (Bauer et al., 2016; Oropeza Bacci et al., 2017). To detect induced seismicity the Aquistore site is equipped with passive seismic monitoring networks including an intermittently deployed array of five downhole geophones (Fig. 1; Nixon et al., 2017) in a deep observation well 150 m to the north-northeast of the injection well; a continuously recording near-surface array of up to 65 geophones and an array of 3–5 broadband seismometers. It has been reported that no significant injection-related seismicity has been observed (White et al., 2017).

Verifying an aseismic response to injection at a site is difficult to achieve because there may always be small magnitude seismic events resulting from fault slip or brittle failure that remain undetected due to low signal-to-noise (SNR) ratios. This study presents a thorough investigation to detect induced brittle failure and fault slip seismic events in the Aquistore passive surface seismic data. In addition, there may be tremour or low frequency long duration (LFLD) events such as those associated with fluid movement in volcanic and industrial settings (e.g., McNutt, 1986). The paper begins with an introduction to the regional geology, followed by an outline of the seismic event detection and location methods used, alongside an analysis of the limitations of these methods. We then attempt to interpret the paucity of induced seismic events within the context of current geomechanical understanding at the site.

2. Regional geology and stress conditions

The Aquistore storage site is in the northern part of the Williston Basin, a regional scale intracratonic basin (Kent and Christopher, 1994) which is 3400 m thick at the site. The basin is outlined according to depth to the top of the Precambrian metamorphic basement in Fig. 2. The basement beneath the basin near the Aquistore site consists of Precambrian metamorphic blocks of the Trans-Hudson Orogen (THO, e.g., Kreis et al., 2000; White et al., 2005) and positive features in the basement are thought to be reactivated fault blocks that controlled facies in the overlying strata (Kent and Christopher, 1994). The Superior and Wyoming cratons constitute the metamorphic basement to the east and west of the THO, respectively.

The Winnipeg and Deadwood formations were chosen as the CO_2 storage reservoir for the project because they are deep, thick clastic sequences of Cambro-Ordovician sandstones. These brine-saturated formations lie at the bottom of the basin's thick Phanerozoic sedimentary succession (Rostron et al., 2014) and rest on the Precambrian metamorphic craton (Fig. 2). Their regional extent provides a vast accessible volume of porous and permeable rock that makes them ideal target reservoirs for CO_2 storage. The overlying strata include a number of low permeability regional seals with the most proximate being the Ice Box Member shale topping the Ordovician Winnipeg Formation and forming the caprock to the CO_2 reservoir, followed by thick evaporite

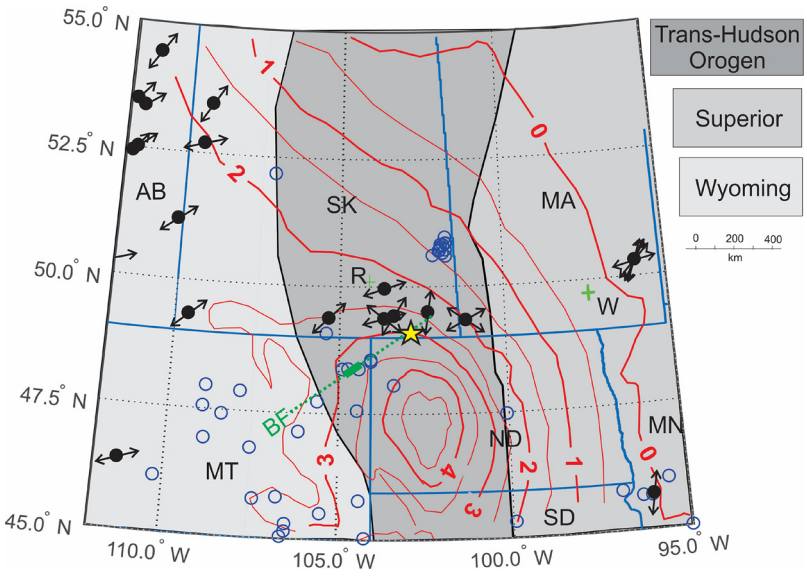

Fig. 2. Regional map centred on the Aquistore site (yellow star) showing thickness contours (red) of the Phanerozoic sedimentary cover above the metamorphic basement in km. Blue open circles indicate epicentres of events with reported magnitudes > 2.5 since 1980. Basement domains are indicated by greyscale shading. The interpreted trend of the Brockton-Froid fault zone (BF) is shown as a green dotted line with its mapped surface expression shown in thick green solid line. Stress direction determinations located at black filled circles with orientation of the maximum horizontal compression indicated by arrows. AB – – Alberta, Sk – Saskatchewan, MA – Manitoba, MN – Minnesota, SD – South Dakota, ND, North Dakota, MT – Montana, R – Regina, W – Winnipeg. (For interpretation of the references to colour in this figure legend, the reader is referred to the web version of this article.)

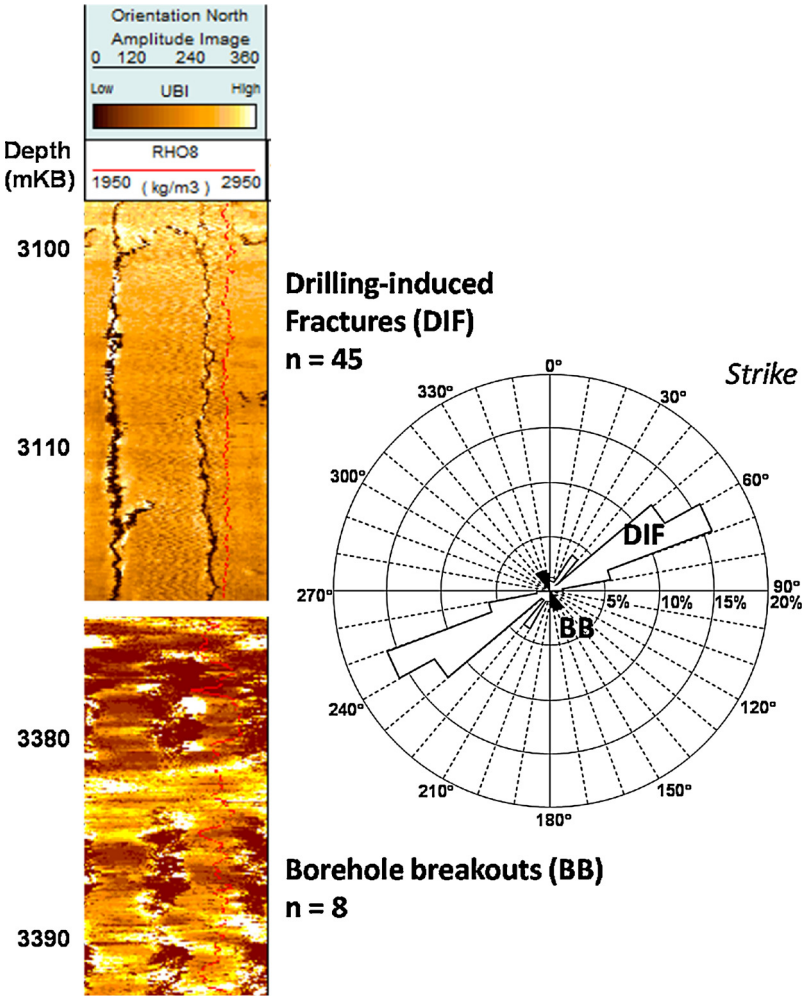

Fig. 3. Left – Static Ultrasonic Borehole Imager (UBI) images from the Aquistore observation well, illustrating drilling-induced tensile fractures and borehole breakouts. Right – Rosette plot summarizing the orientations of drilling-induced fractures (mean azimuth = 59°) and borehole breakouts (mean azimuth = 145°) interpreted for the observation well between 3097 and 3393 m depth. Maximum horizontal stress orientation is parallel to the drilling-induced fractures (shown in white), and normal to the breakouts (shown in black).

sequences of the Devonian Prairie Evaporite Formation. These are effective barriers to CO_2 migration, providing good seal formations for the storage reservoir (White et al., 2016). Further, the CO_2 storage reservoir lies well below the formations hosting economic natural resources in the area, including oil, gas, coal, and potash; and sequestration within the bottom-most Deadwood-Winnipeg sands should not interfere with their extraction.

Natural seismicity in the region is low, as illustrated by the small number of earthquakes since 1980 (epicentres for registered events are shown by the blue open circles in Fig. 2). Horner and Hasegawa (1978) report that, prior to 1978, there were nine events felt in southern Saskatchewan including an earthquake on 15 May 1909, with an estimated magnitude and epicentre of m_b = 5.5 and 49°N 104°W, respectively. To the southwest of Aquistore a linear trend of events in northeastern Montana (Fig. 2) has been linked to the Brockton-Froid fault zone (Frohlich et al., 2015), which is a nearly 50 km long lineament observed in air photos in NE Montana (Thomas, 1974) and in surficial geological mapping (Crone and Wheeler, 2000). Horner and Hasegawa (1978) also report that a felt earthquake caused minor damage in the villages of Froid and Homestead, Montana in 1943. The anomalous cluster of events to the north and east of the Aquistore site below 51°N result from activities associated with potash mining (Gendzwill et al., 1982); the scatter in the lateral positioning of these events is likely indicative of the uncertainties in accurately locating these relatively small, shallow events with the sparse seismometer coverage available when they occurred. Finally, at smaller scales, Jahan et al. (2017) claim to detect two possibly orthogonal fault patterns using attribute analysis of 3D seismic volumes within the Bakken Formation about 100 km to the southeast of Aquistore. Regardless, more recent detailed analyses of EarthScope US Array temporary stations from 2008 to 2011, when densely spaced arrays of seismometers were deployed in the region, detected only 9 events; hence further confirming the aseismic character of this region.

One potential mechanism for induced seismicity during CO_2 injection is through movement on pre-existing faults due to an increase in pore pressure or a change in stress conditions that pushes a fault to failure. However, Verdon et al. (2016) find no evidence in Saskatchewan of induced seismicity due to oilfield activity. As noted above, natural seismicity is low in the area and no major, seismogenic fault zones are located near the site. However, a local sub-vertical Precambrian basement fault was interpreted to exist near the injection well by White et al. (2016), having a NNW-SSE strike direction (10° to 20° counter-clockwise from north). This fault lies beneath a flexure within the overlying Cambrian to Silurian strata. There is no clear evidence that the strata in the flexure are ruptured or faulted, but for simplicity this basement fault and overlying flexure are collectively referred to as a "fault" in this work.

The Williston Basin has seen substantial drilling and hydraulic fracturing into the Bakken unconventional reservoir such that the

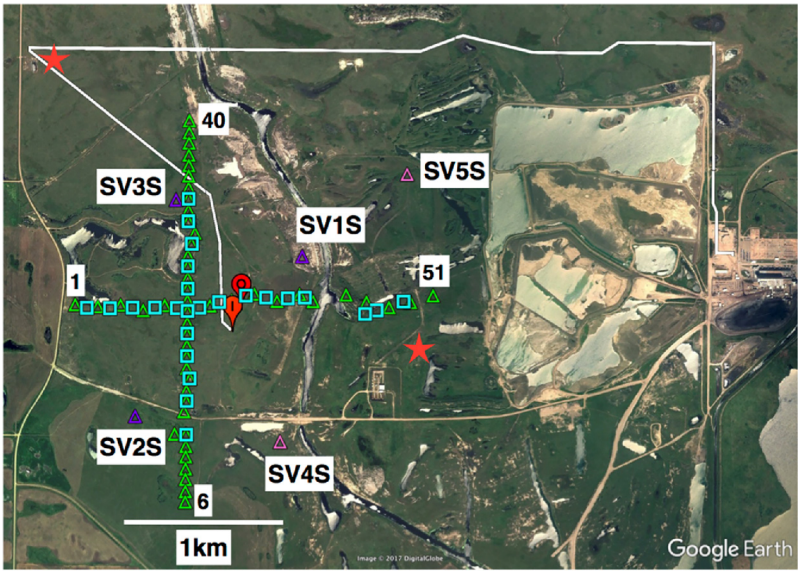

Fig. 4. A Google Earth image of the Aquistore site showing the locations of the seismic monitoring array. Green triangles are the 1C geophone locations, blue squares are the 3C geophone locations, and the initial broadband station locations are shown by the purple triangles with the pink triangles being stations deployed later. The injection and observation wells are indicated by "I" and "O". The pipeline location is shown by the white line, originating at the Boundary Dam power station at the eastern edge of the image. Station labels are referred to in Fig. 9. The red stars are the locations of orientation shots. (For interpretation of the references to colour in this figure legend, the reader is referred to the web version of this article.)

hydrocarbons recovered there now constitute a sizable fraction of total North American production. Despite this high level of industrial activity, there is a paucity of publicly available geomechanical information. There is little available information on stress directions or magnitudes with the available data as accessed from the World Stress Map (Heidbach et al., 2010) supplemented with more recently compiled data for Canada (Reiter et al., 2014) shown in Fig. 2. McLennan et al. (1986) carried out hydraulic fracturing stress determinations from 2062 m to 2215 m depth in a borehole drilled for geothermal exploration in Regina from which they interpreted minimum horizontal stress magnitudes that ranged from 35 to 42 MPa (corresponding to gradients of 15.8–20.4 kPa/m), with hints that the magnitudes in the metamorphic basement discontinuously increased over those in the overlying sediments. They were not able to indicate stress directions. In southeastern Saskatchewan, Hlidek and Rieb (2011) have reported a minimum horizontal stress gradient of 15.4 kPa/m at 1500 m depth for the Bakken Formation, and Hawkes and Gardner (2012) have reported gradients in the 15.9–16.3 kPa range at depths slightly less than 1400 m in the Lower Watrous Formation. An average minimum horizontal stress (i.e., "fracture pressure") of 48 MPa (corresponding to a gradient of 14.9 kPa/m) has been used for operational design purposes at the Aquistore site, though a more detailed treatment of minimum horizontal stress throughout the caprock and injection zone are given later in this paper.

The directions of the maximum horizontal compression S_{Hmax} in Fig. 2 arise primarily from analysis of geophysical logging data that show borehole breakout and drilling induced tensile fracture orientations (Schmitt et al., 2012). The exception to this is the cluster of measured orientations northeast of Winnipeg, these were carried out in the crystalline craton rocks in the Pinawa Underground Research Laboratory using overcoring techniques. The stress orientations in the vicinity of Aquistore are scattered, but it is not known whether this is due to actual stress heterogeneity at what may be the edge of the structural basin or simply due to poor data quality. Analysis of drilling-induced fractures and borehole breakouts observed in ultrasonic image logs in the Aquistore boreholes (see Fig. 3), however, suggest S_{Hmax} trends NE-SW at 65° ± 5°; this is similar to, but somewhat more easterly, than the directions inferred in recent synopses (Bell and Grasby, 2012; Reiter et al., 2014).

Additionally, small seismic events could be expected if CO_2 injection fractures the rock. Such events induced by hydraulic fracturing tend to have magnitudes, M < 1 (e.g., Stork et al., 2015; Goertz-Allmann et al., 2017), making them difficult to detect at the surface if they occur > 3 km deep or if there are high noise levels at the site. As reported above, the fracture pressure at a depth of 3.2 km at the Aquistore site has been estimated as 48 MPa (or a fracture gradient of 14.9 kPa/m). The bottom-hole pressure in the well has not generally exceeded 42 MPa (Pekot, 2016; Jiang et al., 2017) except for three short periods of two days or less in 2015 and therefore it is not expected that injection has caused significant hydraulic fracturing.

3. Seismic monitoring at Aquistore

Extensive passive seismic monitoring experiments have been deployed to study the seismic response of the Aquistore site to injection. These deployments comprise of

a) a permanently recording near-surface deployment of geophones,
b) a continuously recording small array of surface broadband stations,
c) an array of five 3C borehole sondes deployed over the depth range of 2850–2910 m in the observation borehole,
d) intermittent operation of the geophones deployed for the 3D seismic surveys (Roach et al., 2015),
e) a short-term downhole deployment of a DAS fibre-optic cable (Harris et al., 2016).

The position of the downhole geophone array is shown in Fig. 1 and the set-up of the continuously recording near-surface geophone and surface broadband arrays are shown in Fig. 4. The instruments are deployed with the injection well close to the center of the surface arrays. The deployments have operated in various configurations over time with a summary provided in Fig. 5, except for the 3D seismic array and the DAS cable which are not part of this study.

3.1. Near-surface geophone array

The array of 50 10 Hz one-component (1C) geophones was operational at the site years before injection commenced (since July 2012), thus providing an excellent local seismicity baseline for the site. This array consisted of GS-One instruments buried approximately 20 m deep, deployed in one North-South and one East-West line with a spacing of approximately 72 m and each line approximately 2.5 km long (Fig. 4). In October 2014, this array was augmented with 25 GS-One 3C geophones that were installed approximately 6 m below the surface. Some of these replaced 1C instruments so, since 30 January 2015, data is available from a 65-geophone array (Fig. 4) providing continuous data

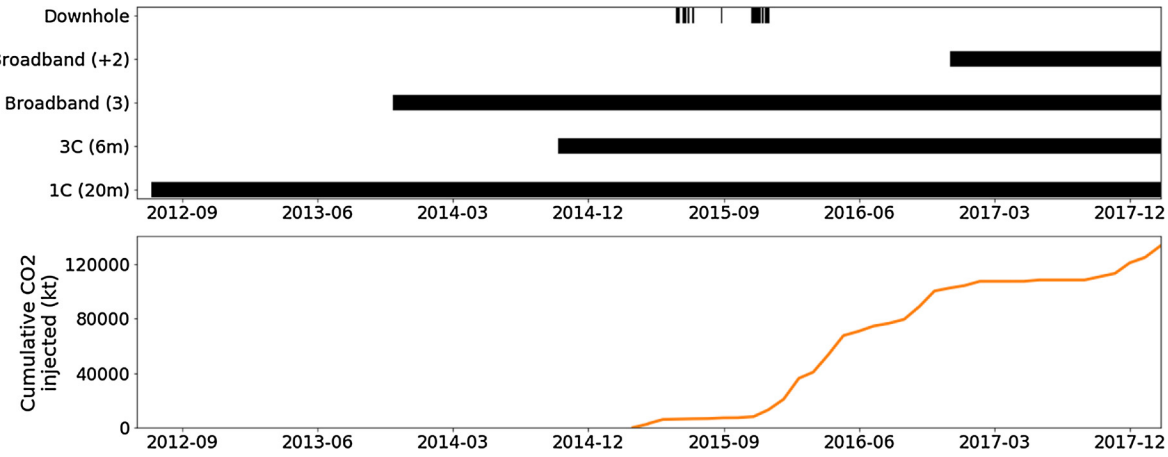

Fig. 5. A Gantt chart of the passive seismic monitoring arrays operational at Aquistore since 2012 (above) and the cumulative CO_2 injection up to February 2018 (below). The arrays consist of 1-component geophones buried 20 m deep; 3-component geophones buried 6 m deep; 3 original broadband stations; 2 additional broadband stations and 5 3C downhole geophones.

with a sample rate of 500 Hz. Data from this array is termed *near-surface data* in the remainder of the paper.

3.2. Surface broadband seismometers

In November 2013 three Güralp GMG-40T (0.1–50 Hz) surface seismometers were deployed distributed in azimuth within about 1 km of the injection well (Fig. 4). In October 2015 one of these sites was replaced with a Nanometrics Trillium Compact 20 s seismometer. Since December 2016, five broadband stations have been operating at the site and the network consists of three Güralp instruments (GMG-40T, CMG-3T, CMG-3ESP) and two Nanometrics Trilliums (Compact 20s and 120P). Data is recorded with a sample rate of 100 Hz and transmitted to the Canadian National Seismograph Network. Data from this array is termed *broadband data* in the remainder of the paper.

3.3. Downhole geophone array

During the first 8 months of injection from May to December 2015, an array of five 15 Hz 3C wall-locking geophone sondes (Sercel Slimwave™) was deployed at depths from 2950 m to 3010 m in the observation well (Fig. 1) (Nixon et al., 2017). The primary purpose of this preliminary placement was to provide detectors in relatively close proximity to the injection point (~3200 m). Low noise levels were achieved because the geophones were well removed from surface cultural sources and their responses digitized directly within each sonde with the data digitally transferred to the surface recording panel. The down-hole digitization is further advantageous in that it avoids noise that arises during analog transmission over such long wirelines. Each of the 15 channels was sampled at 0.5 ms/sample and produced ~11 Gbyte/day, the system condition and snippets of triggered data were monitored remotely daily from Edmonton. In situ conditions of temperature (~115 °C) and borehole fluid pressure (~30 MPa) were challenging and resulted in loss of some of the geophones and locking arm motors during deployment. Frequent tool maintenance was required particularly as those sealing o-rings directly exposed to the wellbore fluid were deformed. Regardless of these difficulties, about 12 weeks of continuously recorded data was obtained during over the deployment period (Fig. 5).

The sonde orientations could not be controlled or measured during installation. Orientation shots from two locations offset > 1.5 km from the well (shown in Fig. 4) were taken in most cases at the beginning and end of each deployment. These dynamite explosions produced clear signals that allowed the sondes to be oriented via hodogram analysis or the two horizontal components on each sonde (e.g., MacBeth, 2002) with an accuracy of better than 0.5° with 95% confidence. In addition to providing clear indication that the system was operational, these shots provided some controlled measures of amplitudes that allow for preliminary estimation of the minimum signals observable as described later. Data from this array is termed *downhole data* in the remainder of the paper.

4. Seismic arrival detection and event location methods

Algorithms to detect and pick seismic arrival times are based on detecting changes in recorded energy. Arrivals may be determined by detecting fluctuations in signal amplitude, frequency content or particle polarisation and one of the most widely used techniques in global seismology and in industrial settings is the short-term average (STA) to long-term average (LTA) ratio (STA/LTA) method (e.g., Allen, 1978, 1982; Baer and Kradolfer, 1987) which identifies changes in amplitude.

If the SNR of a seismic recording is < 1.0 then the signal is unlikely to be visible to the naked eye or to be detected by standard automatic techniques, unless the frequency content of the event and the background noise are substantially different. To detect small events, it may therefore be necessary to use non-standard techniques. Over recent years, significant developments in seismic processing techniques and computational power have occurred to improve event detection using, for example, waveform template matching (e.g., Skoumal et al., 2014), migration-based techniques where the data is stacked to improve SNR (e.g., Chambers et al., 2010) and, most recently, machine learning (e.g., Yoon et al., 2015). However, because such methods are often more computationally expensive and time-consuming than traditional detection methods (e.g., Skoumal et al., 2016 and references therein), they are therefore not currently routinely applied. To analyse the near-surface and broadband data from the Aquistore site we apply the STA/LTA method and also test a simple data stacking technique with the intention of decreasing the event detection threshold. Below we present these detection methods as applied to the Aquistore passive seismic data.

STA/LTA seismic event detection is one of the most commonly applied methods in, and it is therefore applied to the Aquistore data. Using this method seismic wave arrival times may be determined by detecting changes in signal amplitude, frequency content or particle polarisation. These averages may be calculated from the amplitude of the raw seismic trace or using a characteristic function. Some commonly used methods determine the characteristic function for the short-term and long-term windows from the signal envelope (Allen, 1978; Earle and Shearer, 1994) and an arrival is declared when the STA/LTA goes above a specified threshold. For a simple, rolling window STA/LTA the STA

and LTA for window i can be given by

$$STA_i = \frac{1}{M}\sum_{j=L-M+i}^{L+i-1} X_j^2 \quad (1)$$

and

$$LTA_i = \frac{1}{L}\sum_{j=i}^{L+i-1} X_j^2 \quad (2)$$

respectively, where X_j is the trace amplitude, M is the length in samples of the STA window and L is the length in samples of the LTA window. The chosen window sizes depend on the duration and frequency content of the events one wishes to detect, so smaller events will require shorter windows. To increase the speed of the technique a recursive method is often used to avoid keeping large amounts of data in memory so the STA and LTA are calculated using

$$Y_i = \frac{C}{X_i^2} + (1 - C)Y_{i-1} \quad (3)$$

where Y_i is the new average, Y_{i-1} is the average of the previous data point and C is a positive coefficient less than one (Evans and Allen, 1983). This is the method we apply to the Aquistore data.

In addition to the STA/LTA method we also apply data stacking methods to the Aquistore near-surface data to improve detection. Stacking seismic traces from individual receivers in an array can help improve the SNR for detection and for a review of array seismology methods see Rost and Thomas (2002). To successfully sum recordings to improve SNR, the waveforms must be similar. Here we will briefly describe each of the stacking methods tested on the Aquistore array data. In its simplest form data stacking is conducted using a linear stack. In this method, after shifting traces according to the apparent wave velocity across the array, the recordings from all receivers are summed together and the linear stack is given by

$$S_{lin}(t) = \frac{1}{R}\sum_{k=1}^{R} X_k(t) \quad (4)$$

where R is the number of receivers and $X_k(t)$ is the trace amplitude at receiver k at time t. This type of delay-and-sum method is called beamforming in global seismology or migration where the assumption of a plane wave breaks down (Rost and Thomas, 2009).

In this study, we also test other statistical methods to conduct beamforming/migration: N^{th} root; and semblance-weighted stacking. For an N^{th} root stack, the N^{th} root of the data is taken and the traces are summed while preserving the sign of each sample:

$$s_{nth}(t) = \sum_{k=1}^{R} |X_k(t)|^{\frac{1}{N}} . sgn(X_k(t)) \quad (5)$$

where

$$sgn(x) = \begin{cases} -1 \; for \; x < 0 \\ 0 \; for \; x = 0 \\ 1 \; for \; x > 0 \end{cases}.$$

This is then raised to the N^{th} power (Muirhead and Datt, 1976):

$$S_{nth}(t) = |s_{nth}(t)|^N . sgn(s_{nth}(t)) \quad (6)$$

The value of N must be chosen by the analyst and larger values of N result in more significant distortion of the waveform. However, in the presence of uncorrelated noise Nth root stacking performs better than linear stacking because coherent signals are enhanced.

Finally, the semblance stack uses the semblance of a signal to weight a stacked trace. The semblance gives a measure of the similarity of signals and is given by

$$s_{sem}(t) = \frac{\left[\sum_{k=1}^{R} X_k(t)\right]^2}{R\sum_{k=1}^{R} X_k^2(t)} \quad (10)$$

and the semblance-weighted stack is then a combination of a linear stack and semblance (Kennett, 2000),

$$S_{sem}(t) = s_{sem}(t)S_{lin}(t), \quad (11)$$

These techniques have been used effectively to improve seismic phase identification, for example, Castle and Creager (1999) use the N^{th} root algorithm to identify the SP phase from the 660 km discontinuity and Mohan and Rai (1992) apply a semblance technique to image seismic scatterers beneath an array. Such techniques have also been applied to industrial settings to identify previously undetected perforation shots (Chambers et al., 2010) and induced seismic events (Verdon et al., 2017).

In this study, we apply stacking techniques that have proved effective in industrial settings similar to those reported by Chambers et al. (2010) and Verdon et al. (2017). Alternative seismic event detection techniques, not tested here, include waveform cross-correlation (e.g. Gibbons and Ringdal, 2006), frequency-domain processing using changes in power spectral density estimates (e.g. Withers et al., 1998), autoregressive methods (e.g. Sleeman and van Eck, 1999), high-order statistics methods, such as kurtosis and skewness (e.g., Saragiotis et al., 2002; Li et al., 2016) and stacking methods using coalescence mapping (e.g., Drew et al., 2005). See Li et al. (2016) for a summary of proposed event detection methods.

To locate any events detected, we apply the Non-Linear Localization (NonLinLoc) location algorithm (Lomax et al., 2000). The algorithm follows the probabilistic approach to inversion described by Tarantola and Valette (1982) to estimate an event hypocentre and the associated *a posterior* probability density function (PDF). Global sampling methods are possible with this technique (here we use oct-tree sampling) and the solution is nonlinear. The maximum likelihood hypocentre found during the search and the expectation hypocentre (the mean location of the PDF) are both calculated. Probabilistic location uncertainties are given by the confidence volume described by the PDF scatter. The Gaussian location confidence ellipsoids (e.g., 68%) are given for the expectation hypocentre. NonLinLoc has successfully been applied to local and regional studies (e.g., Lomax et al., 2001; Turino et al., 2009) and is an appropriate method for this setting. For location estimates we use a 1D velocity model derived from the 3D P-wave velocity model obtained from a 3D seismic survey and a V_P/V_s of 1.74 (Fig. 6). The dip of geological strata at the site is shallow (~1–2% to the SSE) and therefore the simplified 1D model is considered appropriate for the synthetic tests conducted in this study.

5. Seismic monitoring array performance

Since there have been no seismic events detected that have been attributed to CO_2 injection at Aquistore, in the following section we look at the performance of each seismic monitoring array separately to highlight the detection capabilities and potential limitations of each type of deployment. Two types of event detection are tested. The first is an STA/LTA coincidence trigger. This is tested on all the arrays. The second method is a data stacking and migration technique to detect and locate seismicity. This is tested on the near-surface geophone array.

5.1. Broadband seismic network

We apply the STA/LTA coincidence trigger algorithm from Obspy (Beyreuther et al., 2010) to the broadband array data. To detect any seismicity, we require a trigger at three stations (see Table 1 for parameters used) and apply a recursive STA/LTA algorithm following the methods outlined in Evans and Allen (1983) and Withers et al. (1998).

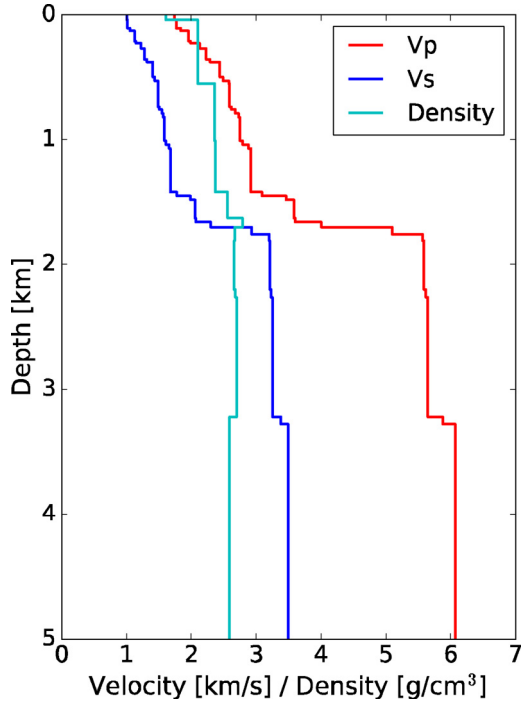

Fig. 6. 1D velocity model for the Aquistore site, derived from the 3D model velocities at the injection well.

Table 1
Automatic event detection parameters used for the broadband stations and near-surface geophones at Aquistore.

	STA length (s)	LTA length (s)	Threshold	# triggers required
Broadband	0.1	2.0	4.0	3
Near-surface geophones	0.1	2.0	6.5	10

The STA and LTA are calculated using Eq. (3) where C is $1/M$ or $1/L$ for the STA and LTA, respectively. The characteristic function is then given by $CF = STA/LTA$. If CF is above a given threshold value a detection is declared.

The broadband seismometers were not deployed when the perforation shots were carried out and the orientation shots are not visible on some or any of the broadband instruments. However, information on blasting in the area between 16 March and 15 June 2015, provided by the Westmoreland Coal Company, is used to test appropriate event detection parameters for the broadband data. During the three-month period 35 events are reported, 31 of which were detected manually. Requiring a coincident trigger on all three broadband stations, we choose a short window of 0.1s and a long window of 2.0s with a threshold of 4.0 (Table 1), detecting 19/35 events and minimising the number of false triggers. Shorter short time windows and a higher detection threshold result in missed detections. Lower detection thresholds result in 100s of false triggers per day and make manual verification a time-consuming job. The chosen parameters result in the detection of onsite anthropogenic activity and nearby seismic events but recordings of teleseismic earthquakes (events at distances > 1500 km from the array) are often missed by the algorithm. This is because the high frequency content has been attenuated and a longer short window would provide improved detection capabilities of teleseismic events.

We do not detect any natural seismicity in the area prior to injection. The STA/LTA coincidence algorithm has also been applied to the available broadband data between April 2015 (when injection began) and March 2018. We detect 315 supposed local mine blasts and 1 near-regional earthquake, with Nuttli (1973) magnitude, M_N, 3.8 at 10:40:51 UTC on 5 September 2016 with epicentre 50.711 N 101.915 W. Depending on noise levels at the site there are between 67 and 2710 triggers per month. Since five stations have been operational it has been possible to reduce the number of false triggers and locate noise sources with more certainty. For example, some triggers are located close to the Boundary Dam power station and are associated with industrial activity on the site (Fig. 7). No induced seismicity associated with CO_2 injection has been identified.

To understand the geomechanical response to CO_2 injection an estimate of seismic event detectability is required. Magnitude of completeness estimates normally require the existence of large event catalogues (Gaucher, 2015). Seismicity in Saskatchewan is sparse (Fig. 2) and so, to estimate the detection capabilities of the broadband array, we use synthetic waveforms added to noise. A period during CO_2 injection but without noise spikes or transient signals (Fig. 8) was chosen to create noise models. The noise models are calculated from broadband recordings using the method of Birnie et al. (2016). In this method the data mean and covariance of the data are used to generate the synthetic noise models by taking random realisations of a multivariate Gaussian distribution. The use of noise models ensures that the data does not contain spikes or transient noise, something which would have to be checked manually on every segment if we were using real noise. Through modelling we can create as much data as required with the same statistical characteristics to test detection capabilities, allowing easy computation of confidence limits and probabilities of detection. The synthetic event waveforms are simple explosion sources with moment magnitudes (M_w) between −1.0 and 1.5 and are computed using E3D, a finite difference elastic seismic wave propagation code (Larsen and Grieger, 1998). A quality factor, Q, of 100 is assumed to account for anelastic attenuation.

To obtain event detection probabilities, we use two-hour-long models and add synthetic events to the noise model at 60 s intervals (119 events) and run an STA/LTA detection algorithm with STA = 0.1s, LTA = 2.0s. For the broadband data, we require a detection on 2/3 stations and use a threshold of 2.8. The thresholds are lower in this test than for the real data due to the lack of transient noise in the model data causing false triggers. For a synthetic event at a depth 3.2 km (the injection depth), the algorithm detects > 95% of events in the broadband data if $M_w \geq 1.3$. Similarly, $M_w \geq 1.0$ events are needed to detect > 10% of events at this depth.

The root-mean-squared (rms) amplitude of the recorded noise is used to estimate the minimum local magnitude, M_L, event that could be detected. In Saskatchewan, the Richter local magnitude scale is used for events with hypocentral distances < 50 km (Bent and Greene, 2014). If it is assumed that events recorded with SNR < 1.0 are not detected, the minimum detectable magnitude on the broadband data for an event with epicentre at the injection well and at 3.2 km deep is M_L-0.8. The estimated detection thresholds can be considered the best performance for the seismic array since any transient noise signals, such as traffic or work on-site, will increase noise levels and potentially cause a deterioration in detection capabilities. Thus, at most times, the actual minimum detectable magnitude is likely to be larger than the values above. It is possible that seismicity is occurring at the site at levels below these detection limits.

To determine the event location capabilities of the broadband array we use arrival times manually picked on synthetic waveforms and NonLinLoc to locate the synthetic events. In the best-case scenario five broadband stations are available and, in this case, for an event at the injection point at a depth of 3.2 km, the estimated event location is within 90 m laterally but only 1.1 km vertically of the true location (Fig. 9). Similarly, for an event at a depth of 2 km the estimated hypocentre is within 90 m (laterally) and 200 m (vertically).

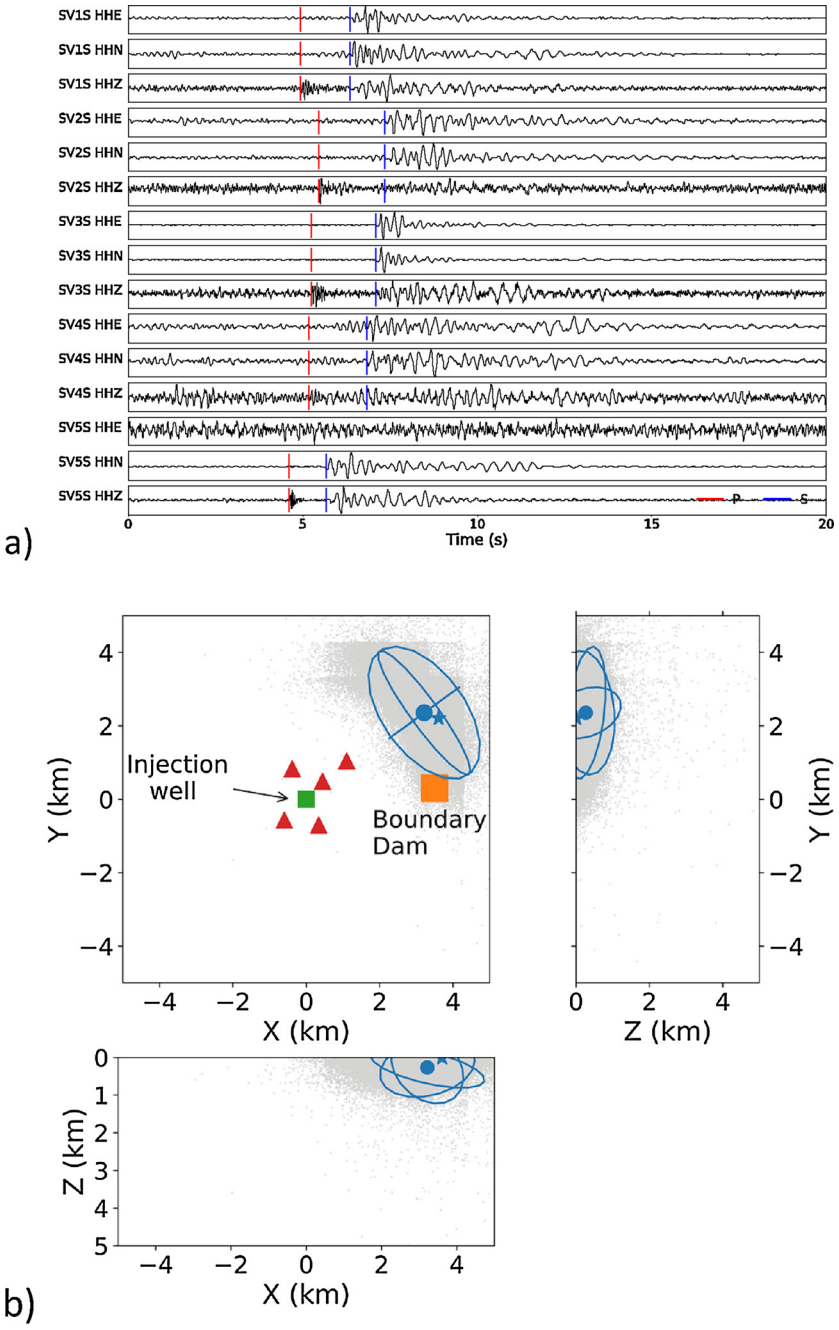

Fig. 7. a) The waveforms recorded at the broadband stations with the *P* (red line) and *S* (blue line) picks for the event located in (b). b) Estimated event location for a trigger on 8 February 2017. The location is estimated using the NonLinLoc program (Lomax et al., 2000). The estimated expectation hypocentre is shown with the corresponding projected 3D 68% confidence error ellipsoid. The maximum likelihood hypocentre is given by the star and the probabilistic location uncertainties are shown by density scatter plots in grey. The red triangles are the broadband seismometer locations. The green square is the injection well. The orange square is the Boundary dam power station. (For interpretation of the references to colour in this figure legend, the reader is referred to the web version of this article.)

5.2. Near-surface geophone array

The same STA/LTA algorithm as used for the broadband array is used to detect events in the near-surface geophone data. With tests similar to those applied to the broadband stations suitable detection parameters are identified (see Table 1). Window lengths of 0.2 s and 2.0 s and a threshold of 6.5 correctly detect 63 supposed mine blasts in the area between April 2015 and February 2016. A coincidence trigger on a minimum of 10 geophones prevents detections due to spurious noise on a few instruments. Calibration data is available in the form of orientation shots and perforation shots. Orientation shots for the 3C near-surface geophones are clearly visible across the array on the geophone recordings (e.g., Fig. 10) and are easily detected by the coincidence trigger algorithm with a range of window lengths. Arrivals from nine perforation shots are also identified with the preferred STA/LTA detection parameters. No local natural seismicity was detected between February 2015 and the start-up of injection in April 2015. No induced seismicity associated with CO_2 injection was identified.

Using noise models created for the geophone data the same method as described above is implemented to study the near-surface array detection capabilities. We use the preferred window lengths, a threshold of 2.7 with triggers required on 10 or more instruments. For a synthetic event at 3.2 km, the algorithm detects > 95% of events if $M_w \geq 0.6$ and 10% of events with $M_w = 0.3$. We also estimate the minimum detectable magnitude as done for the broadband data and find it to be between M_L-1.6 and M_L-0.6, depending on the individual geophone.

Since the near-surface array consists of 10 s of instruments it is possible to test the suitability of data stacking and migration methods to detect seismic events. This is done with the aim of reducing event detection thresholds and identifying any events recorded with SNR ~1.0. We use a beamforming algorithm to obtain the stacked power for the array for a given event location. Using 15s of data, a neighbourhood

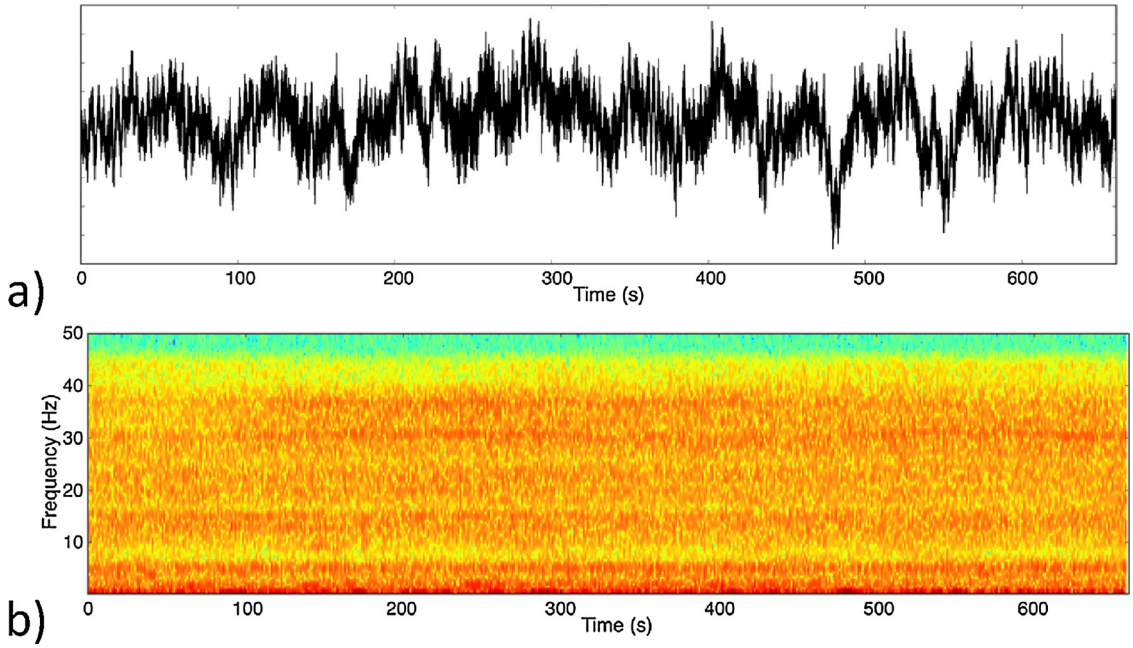

Fig. 8. Seismogram and spectrogram for data recorded at SV3S between 05:37 and 05:48 UTC on 11 May 2015. No significant noise bursts are visible and CO_2 was injected throughout this period.

search algorithm (Sambridge, 1999) is applied to obtain the location with the maximum stacked power and, hence, a potential event location. Initially 500 points are tested within a given volume, chosen as the extent of the array in the horizontal directions and up to a depth of 4 km. Subsequently, the space around the most promising location is resampled. The hypocentre with the highest stacking power is a potential event location. An example of the space sampling and location is shown in Fig. 11. Using the estimated hypocentre, a beamformed STA/LTA characteristic function is produced according to one of the stacking techniques outlined in Section 4 (linear, Nth root or semblance weighted). In fact, there is very little difference between the methods in this case (Fig. 12) because the characteristic function (with only positive values) is being stacked. If the beamformed characteristic function is above a given threshold the data is saved for further inspection to identify any seismic events.

To test this approach, we used synthetic seismograms for an event with an epicentre at the injection well and add them to the geophone background noise models, as described in Section 5.1. We use events with $-1.0 \leq M_w \leq 1.0$, at depths 0.5 km–3.2 km and recorded by between 7 and 47 geophones to test our ability to detect and locate events using stacking of the near-surface array data. For each set of parameters, we add synthetic events to 200 realisations of the noise model.

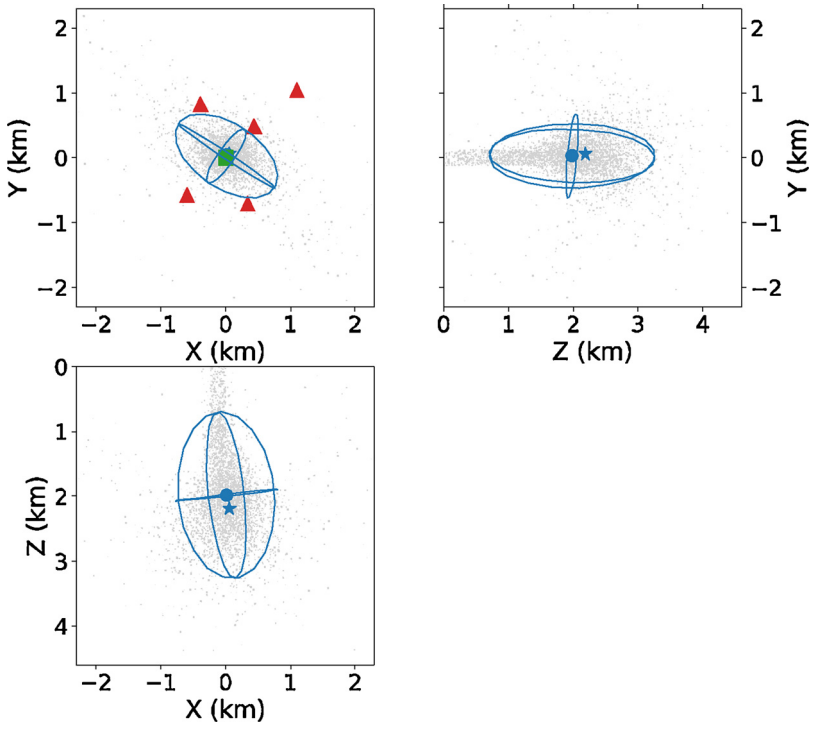

Fig. 9. Estimated event location for a synthetic event at the injection depth (3.2 km). The estimated expectation hypocentre (blue circle) is shown with the corresponding projected 3D 68% confidence error ellipsoid. The maximum likelihood hypocentre is given by the star and the probabilistic location uncertainties are shown by density scatter plots in grey. The red triangles are the broadband seismometer locations. The green square is the injection well. (For interpretation of the references to colour in this figure legend, the reader is referred to the web version of this article.)

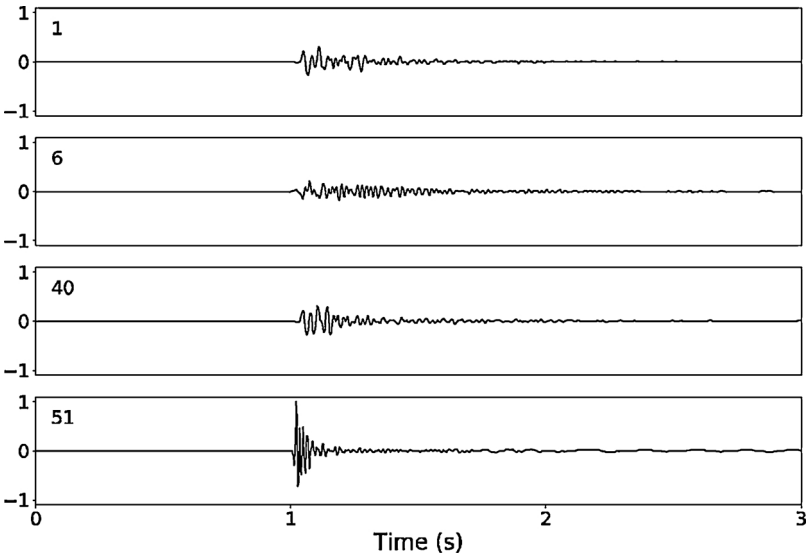

Fig. 10. Geophone recordings from the instruments operating at the expected arrival time of an orientation shot signal. The seismograms cover the full extent of the array (the number indicates the geophone, as given in Fig. 4). Relative amplitudes are shown.

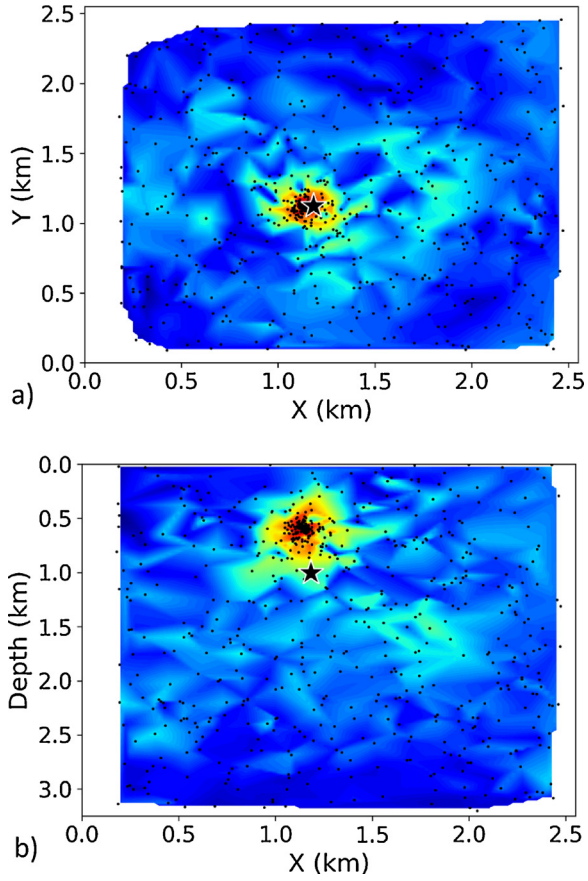

Fig. 11. Example space sampling (black dots) to find the location giving the largest stacked power. Warm colours indicate locations with greater power on the beamformed waveform and the black star is the actual synthetic event location. a) Shows the map view (E-W, N-S) and b) shows the vertical and E-W direction. (For interpretation of the references to colour in this figure legend, the reader is referred to the web version of this article.)

For an event at a depth of 3.2 km, the minimum magnitude reliably detected is M_w0.5. This is a slight improvement in the detection capability reported for the STA/LTA coincidence detection (M_w0.6). To detect a M_w0.0 event it must be shallower than 1.5 km.

The above technique was tested on one month of data following injection start-up (April–May 2015) but no injection induced seismicity was found. With the large data volumes available from Aquistore (a total of 65 geophones recording at 500 Hz), the algorithm as implemented is too slow to be practical for analysis of years of data with a desktop computer (~2/3 real-time). It is ongoing work to apply more computationally efficient methods, such as that developed by Yoon et al. (2015).

Theoretically it is possible to check location capabilities and calibrate the velocity model using the known location of the perforation shots. A total of 13 shots were made in the injection well 14–16 September 2012 when the near-surface array was operating. However, the shots occurred at a time when then instruments required servicing so data is available from a maximum of 14/50 geophones. Only 3 shots were fired when 10 or more geophones were recording. At the time of the best recorded shot 12 geophones were operational but only 5 P- and 4 supposed S-arrivals are visible on the waveforms (Fig. 13a). In fact, the picked S-arrivals are thought to be tube waves because inclusion of these in the location procedure results in significant epicentral errors. Using the P picks only we are able to find the epicentre within 400 m but there is no constraint on the depth (Fig. 13b).

An event hypocentre is estimated as part of the detection process in the stacking algorithm and the errors in the estimated hypocentres in our synthetic tests above are given in Fig. 14a–c. The most significant parameters are those which affect the recorded SNR, namely the event magnitude and depth. Estimated hypocentres are > 500 m from the true location if M < 0.0 or the event depth is > 1.0 km (Figs. 14a and b). The accuracy of estimated hypocentres does not change significantly with the number of geophones, even for small array with 7 geophones, although estimated hypocentre is more variable for smaller arrays (Fig. 14c). The error in depth is the most significant contribution to location inaccuracy, as illustrated if we compare epicentral errors (Figs. 14d–f) with hypocentral errors (Figs. 14a–c).

Our analysis highlights the fact that the inaccuracies in event depth make the most significant contribution to the hypocentral error when using near-surface arrays, as has been widely reported (e.g., Eisner et al., 2009; Maxwell, 2010; Verdon et al., 2012), because there is a direct trade-off between origin time and depth and, here, the aperture of the array is less than the injection depth so changes in event depth of 100 s m result only in small changes in S-P arrival times. A combined downhole and surface survey would be required to reduce the hypocentral errors reported above. This is ongoing work. We also conclude

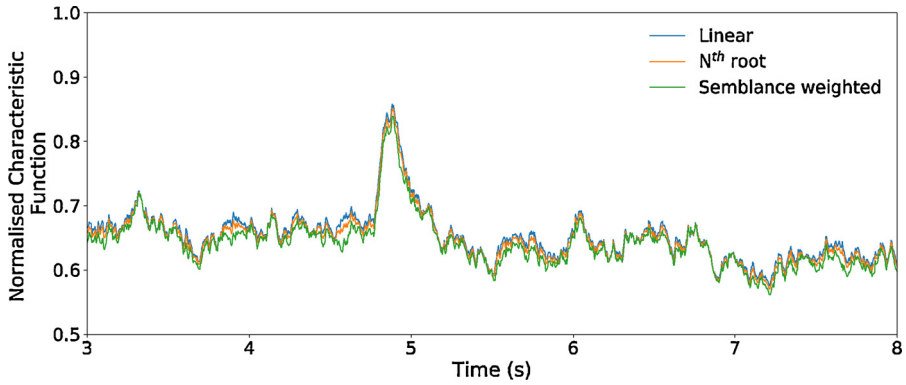

Fig. 12. Example normalised stacked STA/LTA characteristic functions (CF) from synthetic geophone array waveforms for an M_w0.5 event with a hypocentre at the injection well and 3.2 km deep with a first arrival time at 4.9s. Examples of a linear stack; an *N*th root stack and a semblance weighted stack are shown.

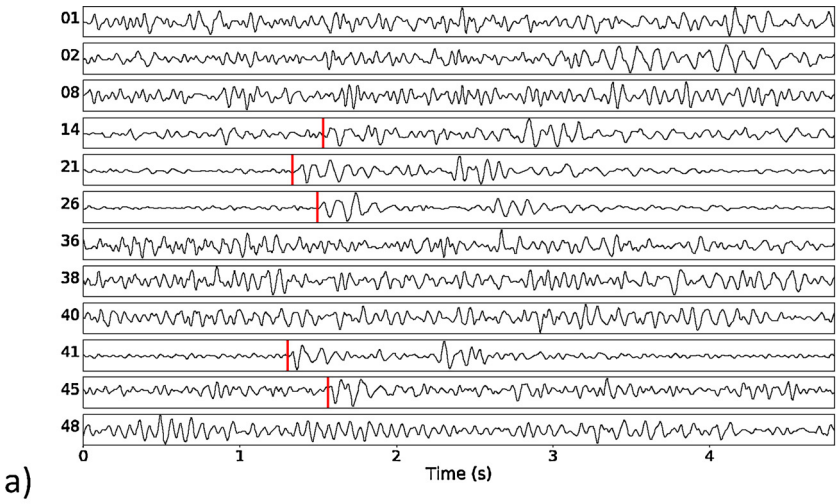

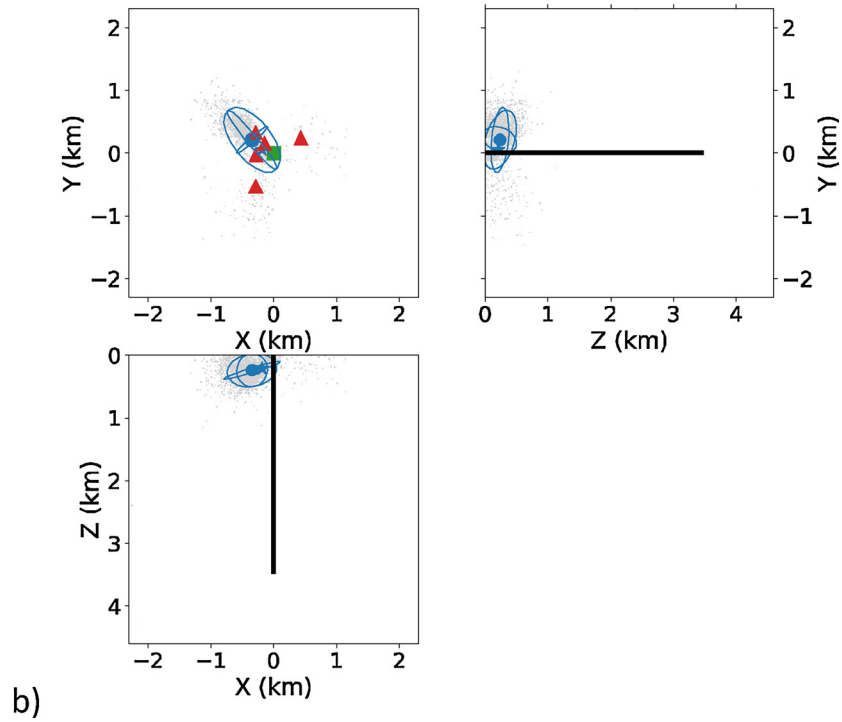

Fig. 13. a) Recorded waveforms of a perforation shot. Data from all operational geophones are shown. Picked P arrival times are indicated by red lines. b) Perforation shot location estimated using NonLinLoc (Lomax et al., 2000) and the P-arrival times picked in (a). The estimated expectation hypocentre is shown with the corresponding projected 3D 68% confidence error ellipsoid. The maximum likelihood hypocentre is given by the star and the probabilistic location uncertainties are shown by density scatter plots in grey. The red triangles are the geophones with available arrival times, the green square is the injection well epicentre. The injection well is indicated by the black line. (For interpretation of the references to colour in this figure legend, the reader is referred to the web version of this article.)

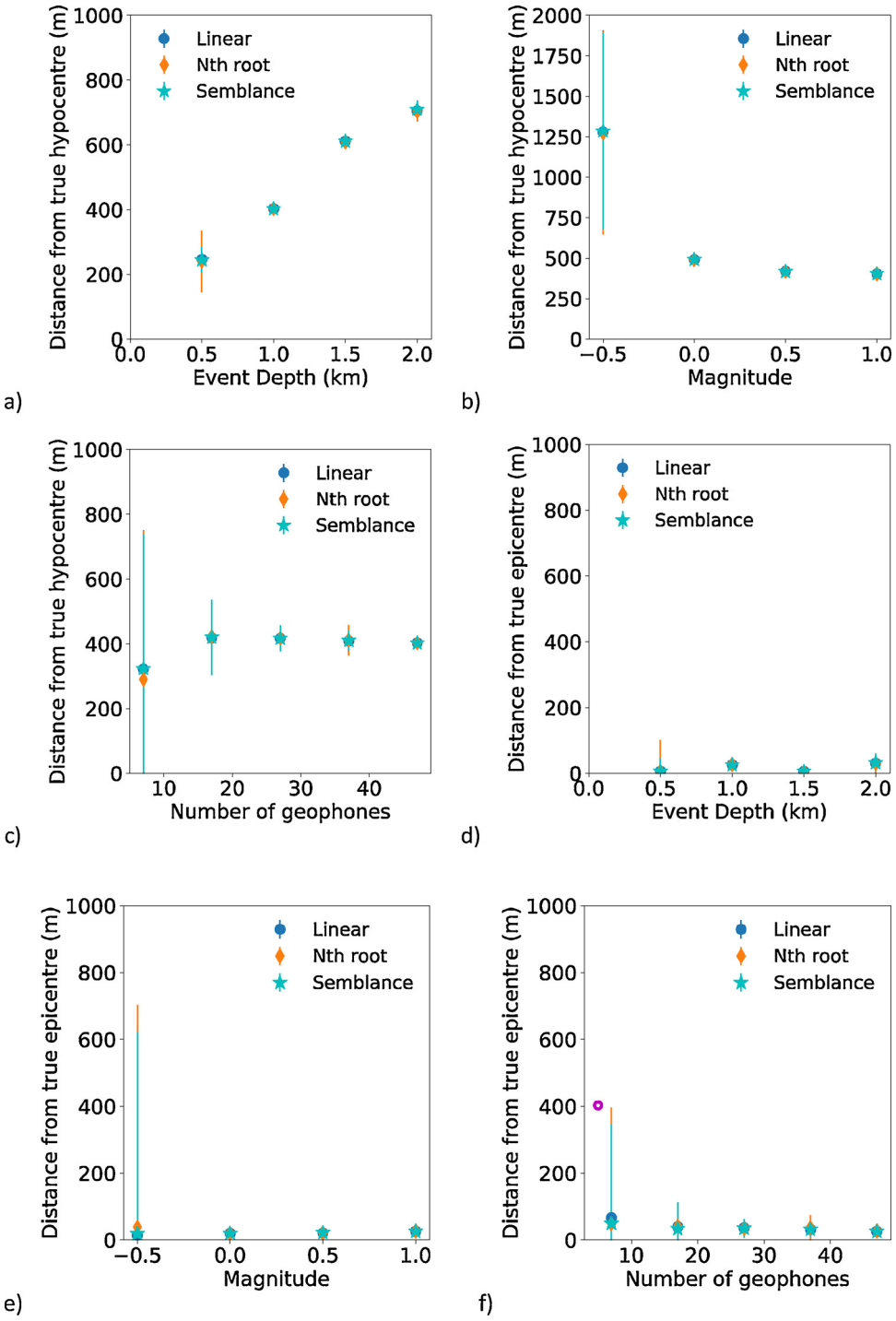

Fig. 14. Errors in hypocentres estimated using a stacking algorithm as a function of a) event depth for an M_w1.0 event recorded by 47 geophones; b) event magnitude for a 1 km deep event recorded by 47 geophones and c) the number of geophones in the array for an M_w1.0 event at 1 km deep. d) – f) As (a)–(c) but with epicentral errors shown. Results are displayed for linear, N^{th} root and semblance-weighted stacking. The error bars are the standard deviation of 200 realisations of the stacking algorithm. The error in the estimated location for the synthetic event reported above is shown for comparison in (f) by the magenta open circle.

that we are unable to comment on the accuracy of the velocity model without further, better recorded, ground truth events (e.g., perforation shots).

5.3. Downhole geophone array

Owing to the prevalence of frequent tube waves in the borehole water column, STA/LTA detection algorithms generate frequent false events. However, due to the low noise levels at 2900 m depth, manual event detection was possible. 900 events of scientific interest were identified in the 12 weeks of monitoring data, however none of these have, as yet, been clearly identified as being related to the injection. That said, the geophones did reliably record other events such as mine blasting and the orientation shots, giving confidence that the system was fully operational. Additionally, even though geophones deployed have lower sensitivity below 15 Hz, a teleseismic event was detected on 30 May, 2015 (M7.8, 189 km WNW of Chichi-Shima, Japan). The inventory of manually selected events is currently being compared to

STA/LTA and other automated detection algorithms. Given the proximity of the downhole array to the injection locations where the rock mass is subject to rapidly increased pore pressures and thermal stress variations, the lack of detectable events was unexpected and we are currently working to better quantitatively assess the minimum detection levels for these instruments.

6. Predicted seismic response from modelled geomechanical response

Injection of fluids into porous rocks that are either immediately above or in direct pressure communication with the Precambrian basement has the potential to induce seismicity (e.g., Kim, 2013; Verdon, 2014). The induced seismicity usually results from the reactivation (shear failure) of existing basement faults that is caused by a reduction in effective normal stress across the fault due to increased pore pressure (e.g., Hubbert and Rubey, 1959) associated with the fluid injection. The likelihood that the fault identified by White et al. (2016) could be reactivated during CO_2 injection is controlled by the effective in-situ stresses acting on it, which in turn are a function of fault orientation, pore pressure and in-situ stress magnitudes and orientations. (The induced temperature change in the vicinity of the fault would be negligible; hence the focus on pressure change for this analysis.) In order to assess the risk of fault reactivation, these parameters were estimated and used for Coulomb failure analysis following standard methods (e.g., Zoback, 2007; Schmitt, 2014). Fault cohesion was assumed to be 0 MPa for these analyses, and the fault friction angle was assumed to be 30° (i.e., the friction coefficient equals 0.58).

According to White et al. (2016), the fault is subvertical and has a strike direction between 10° and 20° counter-clockwise from north, and it transects Precambrian basement rocks and overlying strata up to the Winnipegosis Formation. In this work, it was modelled as a vertical fault with a strike 15° counter-clockwise from north, extending vertically across the entire model domain (which includes the uppermost 20 m of Precambrian basement rocks, the entire Deadwood formation, and the Black Island member of the Winnipeg Formation).

Initial pore pressures have previously been estimated from well tests and used as input for dynamic reservoir simulations (Jiang et al., 2017). Outputs showing predicted pore pressures in the vicinity of the Aquistore injection well and the fault of interest are shown in Fig. 15. The contour plots shown in Fig. 15a depict pressures on January 19, 2016. As shown in Fig. 15b, conditions on this date are representative of the highest pressures achieved during the time interval analyzed. Pressures on December 2, 2015 are also highlighted in Fig. 15b. This is the date of maximum pressure increase experienced while the downhole array was deployed.

Fig. 16 shows a depth profile of vertical stress magnitude calculated from the injection well's bulk density log, supplemented with bulk density log data from an offset well (01/15-15-001-09W2/00) that was logged to shallow depths. This figure also shows elastic properties calculated from sonic scanner log data, and horizontal stress magnitudes calculated using the following equations (based on Warpinski (1989), assuming unidirectional tectonic strain and linear elastic constitutive behaviour):

$$S_{H\,\min} = \frac{\upsilon}{1-\upsilon} S_V + \frac{1-2\upsilon}{1-\upsilon}\alpha p_{fm} + \frac{\upsilon E \varepsilon_{H\,\max}}{1-\upsilon^2} \quad (12)$$

$$S_{H\,\max} = \frac{\upsilon}{1-\upsilon} S_V + \frac{1-2\upsilon}{1-\upsilon}\alpha p_{fm} + \frac{E \varepsilon_{H\,\max}}{1-\upsilon^2} \quad (13)$$

where:

S_V = vertical (overburden) in-situ stress
υ = static Poisson's ratio
a = Biot's coefficient
p_{fm} = formation pore pressure
E = static Young's modulus
ε_{Hmax} = tectonic strain parallel to the maximum horizontal stress azimuth (ε_{Hmin} assumed 0)

Use of sonic logs in estimating stress has become common only because in many cases proper open hole pressure transient tests are not carried out; and some care must be exercised in the use of the values provided. Indeed, Warpinski (1989) indicated that use of these methods can lead to erroneous interpretations if the underlying assumptions are not properly accounted for. Recent studies of rock anisotropy (Ong et al., 2016; Melendez-Martinez and Schmitt, 2016) too indicate issues that can arise in estimating horizontal stresses using sonic log derived values of Poisson's ratio in transversely isotropic rock. Below, we have attempted to adjust the log derived estimates using values of S_{Hmin} obtained from minifrac records.

The elastic properties calculated from log data are dynamic properties, whereas Eqs. (12) and (13) require static properties. Based on a compilation of empirical correlations between static and dynamic Young's moduli, static Young's moduli were estimated as 0.5 times the dynamic (log-derived) values, and dynamic Poisson's ratios calculated from logs were deemed a reasonable approximation for static values (Evans, 1973).

Two scenarios were considered in this work. In Scenario 1, Biot's coefficient was assumed to be 1. Using this assumption, the only way to obtain a minimum horizontal stress similar in magnitude to the fracture closure pressure interpreted from a wireline micro fracture test that was conducted at 3140 m depth (in the Ice Box shale) was to set the tectonic strain to zero. If this were true, the in-situ horizontal stress state would be isotropic. However, the presence of drilling-induced tensile fractures and borehole breakouts in UBI logs obtained in the injection and observation wells (see Fig. 3) suggests that horizontal stresses are in fact anisotropic. Thus, a second scenario was considered, in which Biot's coefficient was assigned a value of 0.9 and the tectonic strain assigned a value of 0.00045. These values provided the best match between calculated S_{Hmin} and the measured fracture closure pressure (49.3 MPa, corresponding to a gradient of 15.7 kPa/m), and calculated S_{Hmax} and the S_{Hmax} value (56.9 MPa, corresponding to a gradient of 18.1 kPa/m) estimated from the fracture breakdown pressure using the following equation (based on Haimson and Fairhurst, 1969, assuming a non-penetrating fluid, linear elastic rock response, a circular borehole drilled parallel to a principal stress direction (S_V), and negligible thermally-induced stresses):

$$S_{Hmax} = 3S_{Hmin} - p_b - p_{fm} + T \quad (14)$$

Where

P_b = fracture breakdown pressure
S_{Hmax} = maximum horizontal stress magnitude
S_{Hmin} = minimum horizontal stress magnitude
p_{fm} = formation pore pressure
T = tensile strength (assumed negligible in this analysis)

Scenario 2 was deemed most reasonable because it better matched the observed horizontal stress anisotropy. Also, this scenario yielded maximum horizontal stresses with upper bound values similar to the vertical stresses, which is consistent with the regional stress regime interpretations that place southeast Saskatchewan as transitional between transpressional (strike slip) and extensional (normal fault) (Bell and Babcock, 1986).

Fig. 17 shows the critical pore pressure required to reactivate the fault, along with the modelled pore pressures at the fault on December 2, 2015 and January 19, 2016. As shown in this figure, the modelled pore pressures for both dates are significantly lower than the critical pressure for fault reactivation. In spite of this favourable scenario, the interpreted basement fault and overlying flexure will clearly be targets of interest during monitoring of CO_2 injection over the longer term, as pressures increase further.

Further to the potential for seismicity induced by reactivation (shear failure) of faults, small seismic events could also occur if CO_2 injection

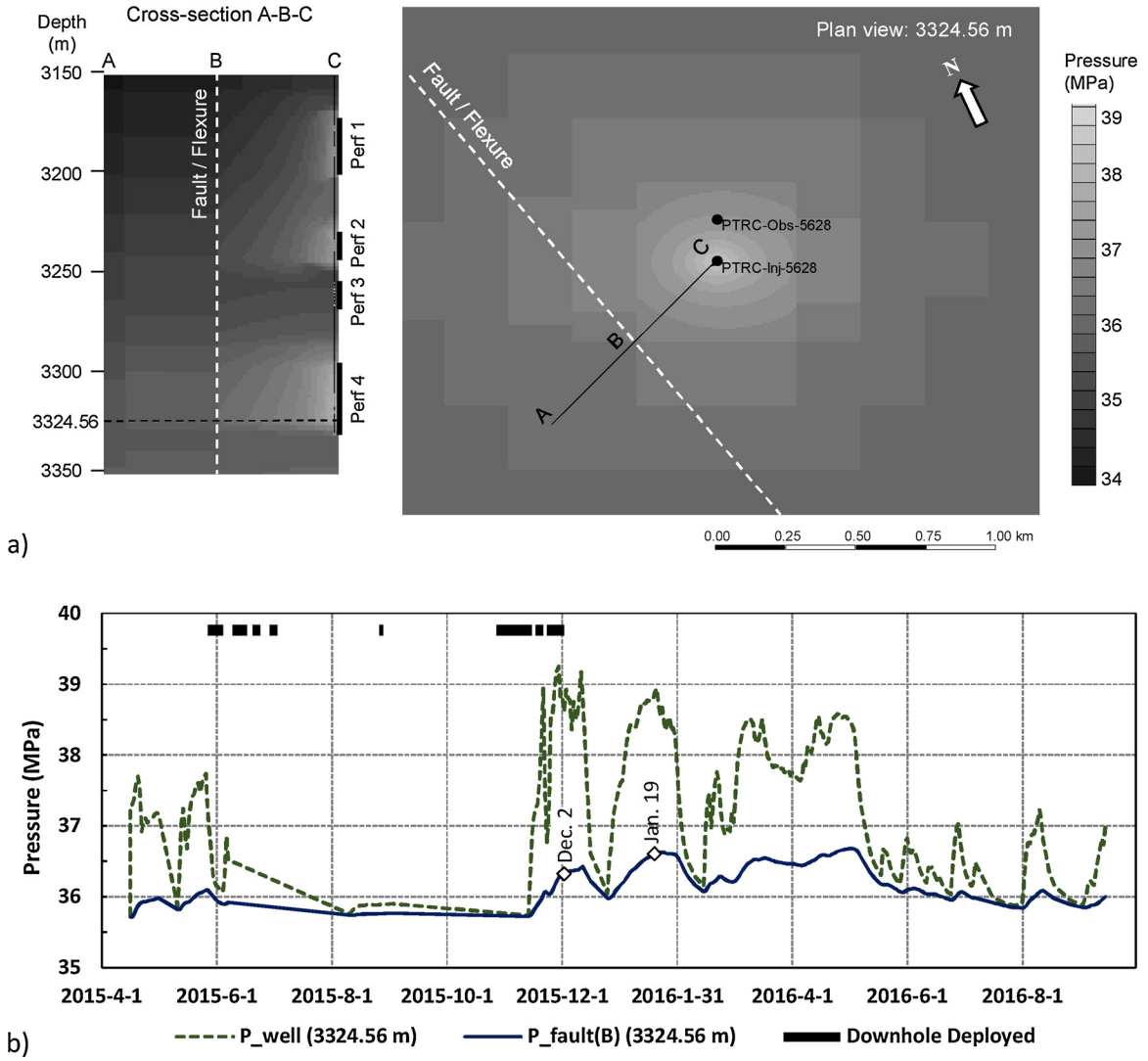

Fig. 15. a) Predicted pore pressure distribution in the general vicinity of the Aquistore injection well and nearby fault on January 19, 2016. Left image shows cross-sectional view, spanning all four perforated intervals of the injection well. Right image show plan view near the base of perforated zone #4, where pressure increase is greatest. b) Graph of predicted pressures in the near-well area and at the fault (point B), at a depth of 3324.56 m (near the base of perforated zone #4). Simulation results generated using the history-matched model presented in Jiang et al. (2017).

induces localized tensile fractures in the vicinity of the injection well's perforated zones. Coupled thermo-poro-mechanical modelling of CO_2 injection is currently in progress. It is anticipated that this modelling will predict localized fracturing as a consequence of elevated pressures and relatively low temperatures near the injection well. However, the evidence collected to date suggests that the magnitudes of micro-seismic events associated with these localized fractures are below the detection limits of the monitoring systems in place (i.e.,$\lesssim M_L$-0.8 for the broadband and $\lesssim M_L$-1.6 for the near-surface geophones).

7. Discussion

An analysis of passive seismic data collected at the Aquistore site between April 2015 and March 2018 has not identified any induced seismicity associated with CO_2 injection. The lack of induced seismicity must be considered in the context of the injection parameters, pressure and temperature changes as a result of injection and detection limits of the seismic arrays deployed at the site. There are several possible explanations for an absence of observed seismicity:

1) Injection has generally been below fracture pressure and therefore should not necessarily induce seismicity.
2) The deviatoric stress is small so that shear failure has not occurred even when fracture pressure is exceeded.
3) Critically stressed fractures/faults are absent or the orientation of existing fractures/faults is not optimal for reactivation with reduced effective stress.
4) Stress release has occurred as a series of many small events below the detection threshold.
5) Stress release has occurred in the form of LFLD events.

Compared to other projects injecting CO_2 into the basal Cambrian sandstone (e.g., Illinois Basin-Decatur Project (Finley et al., 2013) and the Quest CCS project (Bourne et al., 2014)) a relatively small mass of CO_2 has been injected at Aquistore since injection started in April 2015. At Aquistore injection has occurred at highly variable rates ranging from 0 to a maximum of ~2000 t/day, punctuated by periods where the well has been shut-in (i.e. no injection). Maximum injection pressures have generally been at < 90% of the estimated fracture pressure (48 MPa) (Pekot, 2016; Jiang et al., 2017) although there were three short periods of up to 2 days in May and June 2015 when the bottom hole pressure exceeded 48 MPa with the approval of the regulator.

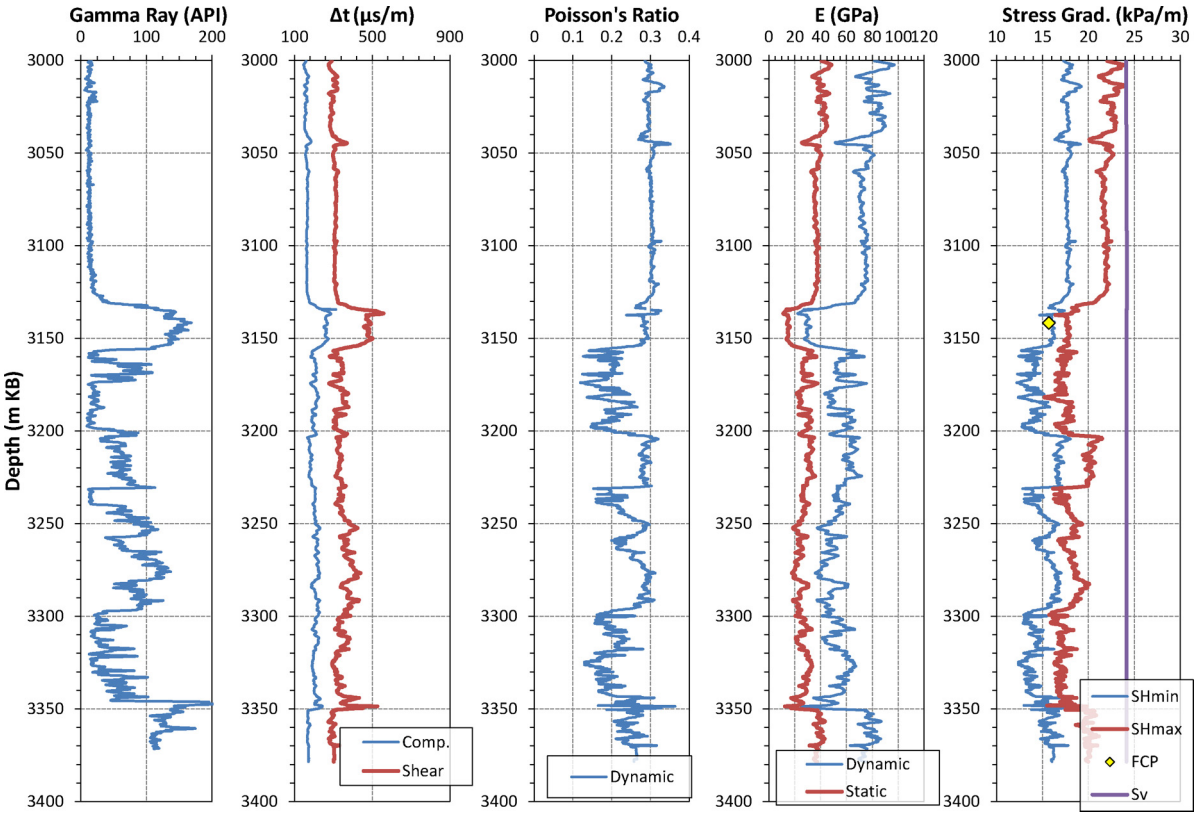

Fig. 16. Wireline log data, calculated mechanical properties, and calculated stresses for Scenario 2 (tectonic strain ε_{Hmax} = 0.00045 and Biot's coefficient = 0.9).

These times were outside the periods of operation of the downhole array and therefore any small magnitude (M < −1.0) hydraulic fracturing events have so far gone undetected.

The Decatur and Quest projects have both reported induced seismicity related to injection but there are important differences between these projects and Aquistore. Decatur and Quest have injected much larger quantities of CO_2 (> 1 Mt) at average rates of ~1000 t/day (Decatur) and ~3000 t/day (Quest). Significant microseismicity at Decatur has been documented with > 5000 events of magnitude −3.0 to 1.2 (with 94% < M0.0 (Kaven et al., 2015; Will et al., 2016; Bauer

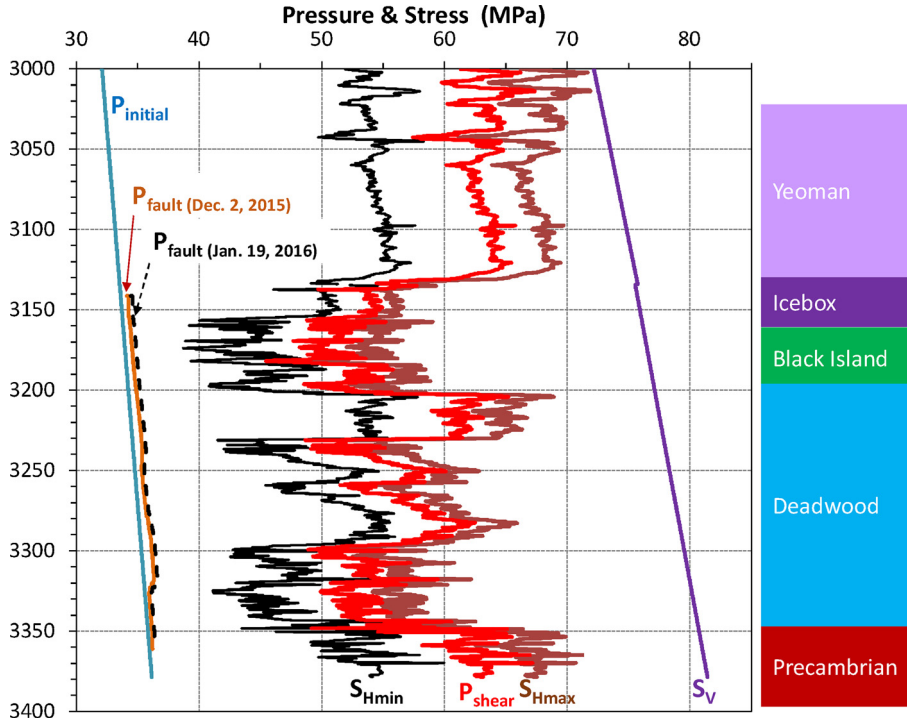

Fig. 17. Comparison of maximum pore pressure near the fault during injection (P_{fault}), as modelled for December 2, 2015 and January 19, 2016,against the critical pressure required to induce shear failure on the fault (P_{shear}).

et al., 2016; Goertz-Allmann et al., 2017). The onset of activity began after 2 months of injection (~56 ktonnes at average injection rates). At the Quest project, there has been a minimal seismic response. The first locatable microseismic event was recorded 9 months after the start of injection (~750 ktonnes using the mean injection rate) and a total of only three locatable events were detected up to 14 months post-injection start-up with magnitudes ranging from Mw −1.8 to −0.6 (Oropeza Bacci et al., 2017). The events occurred in the Precambrian basement, well beyond the extent of the CO_2 plume. Both projects report only small changes in pressure. At the Decatur site injection pressures remained far below fracture pressure during injection (Bauer et al., 2016); the maximum pressure increase is 1.14 MPa or 5.2% above original formation pressures as measured 307 m from the injection borehole or ~65% of the fracture pressure for the injection zone. Similarly, at Quest pressure increases have been small (< 1 MPa) but the pressure response was seen very quickly (within a couple of days) at wells ~5 km from the injection well (O'Brien and Rock, 2016). This indicates there is good connectivity in the basal sandstone and therefore it is not surprising that little microseismic activity has been detected.

In comparing Aquistore microseismicity with these other sites, it is recognized that the monitoring systems at the Decatur and Quest sites have lower magnitude detection threshold values for induced microseisms; $M_w > -0.5$ (Kaven et al., 2015) to $M_w > -2.0$ (Bauer et al., 2016), and $M_w > -1.8$ (Oropeza Bacci et al., 2017), respectively. However, at each of these other sites there are a subset of reported events with magnitudes that would exceed the detection threshold of the continuous monitoring system at the Aquistore site. Furthermore, lower detection threshold values were provided at the Aquistore site during operation of the downhole array at time intervals totaling 12 of the first 30 weeks of CO_2 injection. Thus, it is likely that low magnitude events ($M < -1.0$) would have been sampled during this time if the microseismic occurrence rate was comparable to that observed at the Decatur site. Thus, we conclude that the absence to date of any detectable microseismicity at the Aquistore site is not just an artefact of the lower relative sensitivity of the monitoring system there, but is a characteristic of the site.

Considering the experience at these other comparable projects, there are some common observations:

1) A delay in induced seismicity following the start of injection;
2) Initial seismicity occurs well away (100's–1000's of m) from the point of injection;
3) Seismicity occurs well beyond the estimated/observed CO_2 front;
4) Seismicity can occur for pressures that are well below the fracture pressure.

These observations suggest that the onset of detectable seismicity (for injection below fracture pressure) may be controlled by the time that it takes the pressure field to diffuse to locations where pre-existing "critically-stressed" fractures/faults/weaknesses can be activated by the pressure perturbation. This leads to perhaps the simplest explanation for the lack of induced seismicity at the Aquistore site being the small mass (volume) of CO_2 injected to date. This limits the magnitude of the pressure perturbation as well as the distance to which it extends. Furthermore, the sporadic nature of injection at the Aquistore site could allow relaxation of the pressure plume during non-injection periods. This, in turn, could limit the magnitude of the pressure perturbation seen at a location away from the injection well. Indeed, the largest modelled pore pressure perturbations during injection are < 1 MPa > 500 m from the injection well (Fig. 15).

The detection limits of the seismic array deployments limit the extent to which it can be said injection is aseismic at Aquistore. This study presents a thorough investigation of the seismic event detection capabilities at the site. Recordings of known events (mine blasts, local earthquakes, perforation shots, orientation shots) are used to determine suitable detection parameters for STA/LTA analysis. Since these parameters have been determined without any seismicity observed at the Aquistore site, they may require adjustment if any such events are ever detected and should be kept under review. Methods to improve SNR and detection by stacking waveforms have also been assessed for the near-surface geophone array. Tests with synthetic waveforms indicate a slightly improved event detection threshold of $M_w0.5$ over the standard STA/LTA technique ($M_w0.6$) for an event hypocentre at the injection point.

An analysis of noise recorded during a quiet period without noise spikes, suggests a $M_L > -0.8$ event may be detected on the broadband station recordings, compared to a minimum event magnitude of M_L-1.6 for the near-surface geophones. These values represent minimum detectable magnitudes and during periods of transient noise (e.g., while work is occurring onsite) the detection threshold will deteriorate. Although our analysis suggests injection has been aseismic at Aquistore, there remains the possibility that $M_w < 0.0$ events have gone undetected during noisy times or when instruments were not functioning. Estimates of the detection threshold for the downhole geophones are ongoing. Research into alternative event detection methods is also ongoing. Techniques such as energy back projection (e.g. Inbal et al., 2015), tomographic fracture imaging (e.g., Ross et al., 2017) or machine learning techniques (e.g., Yoon et al., 2015) may provide useful information and improve detection capabilities.

Considering monitoring for future CO_2 storage projects, the small array of broadband seismometers provides a relatively cheap and easy to deploy array for passive seismic monitoring. This makes this type of deployment an attractive prospect if the desired detection threshold is met. The minimum detectable magnitude for an event at the injection depth is estimated to be approximately M_L-0.8 for the Aquistore broadband array. This is comparable to the detection threshold of the near-surface geophones given the minimum detectable magnitude for these geophones varies by one magnitude unit, depending on the individual instrument. To confirm detection of a seismic event, *P*-arrivals must be identified at multiple stations. Initially only three broadband stations were deployed and, for event detection, a coincidence detection on only two stations was tested. This results in a large number of false triggers and requiring a detection on all three stations significantly reduces the number of these false triggers. However, this also decreases the likelihood of detecting a seismic event if one station is noisy or not functioning as expected. Since five broadband stations have been deployed it has been possible to reduce the number of false triggers and improve event location capabilities. In future deployments, a network of at least five stations should be deployed, not only to allow for transient noise on some stations but also because arrival times from at least three stations are required to estimate event hypocentres with sufficient accuracy so as to be useful to make a geomechanical and geological interpretation of the processes occurring with injection.

8. Conclusions

Multiple seismic monitoring arrays have been deployed at the Aquistore site to determine whether CO_2 injection is inducing seismic events, important information for the hazard assessment of the project. A careful analysis of geophone and broadband seismometer data has not revealed any induced seismicity considered to be related to injection. Analysis of this data is ongoing and the potential for combined data analysis will be useful if seismicity is detected.

The estimated minimum detectable magnitude for the broadband stations for an event with an epicentre at the injection well occurring at the injection depth (3.2 km) is M_L-0.8. With an estimated minimum detectable magnitude between −1.6 and −0.6, the detection capabilities of the near-surface geophone array are better than the broadband stations because they are buried and have lower noise levels. In addition to the widely-used STA/LTA detection method, the ability of the geophone array to detect events was tested using data stacking methods. It was found that the array could reliably detect events with

M_w0.5 and at a depth of 3.2 km. We estimate an $M_w \geq 0.6$ event would be detected in the near-surface geophone array data with a probability of > 95% using STA/LTA detection and events $M_w \geq 1.3$ would be detected with the broadband array. Seismicity may be occurring at the site at levels below these detection limits.

Geomechanical modelling suggests insignificant effective stress changes at the identified fault near the Aquistore injection well. Moreover, this fault is oriented sub-parallel to a principal stress direction (SH_{min}), thus the shear stresses acting on it are relatively small. However, continued monitoring of pressures near this fault are recommended, as the risk of reactivation (and induced seismicity) will increase as larger volumes of CO_2 are injected. Similarly, more investigation is required to predict the likelihood of small induced seismic events resulting from localized tensile fracturing due to injection pressures similar in magnitude to the fracture pressures, especially when accounting for the reduction in fracture pressure resulting from thermally-induced stresses (when CO_2 temperatures are cooler than the native formation temperature).

Acknowledgements

The authors gratefully acknowledge the Petroleum Technology Research Centre's (PTRC's) Aquistore Project for its support and collaboration on this research. ALS acknowledges the financial support of the UK CCS Research Centre (www.ukccsrc.ac.uk) in carrying out this work. The UKCCSRC is funded by the EPSRC as part of the RCUK Energy Programme (EP/K000446/1). ALS thanks the Bristol University Microseismicity Projects (BUMPS) sponsors for supporting this research. Third party data was used in this study. Access to the geophone array data can be applied for from PTRC. The broadband station data is available from NRCan. We thank two anonymous reviewers for their comments that helped improve this manuscript. This is Geological Survey of Canada contribution 20180037.

References

Allen, R.V., 1978. Automatic earthquake recognition and timing from single traces. Bull. Seis. Soc. Am. 68, 1521–1532.
Allen, R., 1982. Automatic phase pickers: their present use and future prospects. Bull. Seis. Soc. Am. 72, S225–S242.
Baer, M., Kradolfer, U., 1987. An automatic phase picker for local and teleseismic events. Bull. Seis. Soc. Am. 77, 1437–1445.
Bauer, R.A., Carney, M., Finley, R.J., 2016. Overview of microseismic response to CO2 injection into the Mt.Simon saline reservoir at the Illinois Basin-Decatur Project. Int. J. Greenhouse Gas Cont. 54, 378–388. http://dx.doi.org/10.1016/j.ijggc.2015.12.015.
Bell, J.S., Babcock, E.A., 1986. The stress regime of the Western Canadian Basin and implications for hydrocarbon production. Bull. Can. Petrol. Geol. 34 (3), 364–378.
Bell, J.S., Grasby, S.E., 2012. The stress regime of the Western Canadian Sedimentary Basin. Geofluids 12, 150–165.
Bent, A., Greene, H., 2014. Toward an improved understanding of the M_N-M_w time dependence in eastern Canada. Bull. Seis. Soc. Am. 104, 2125–2132.
Beyreuther, M., Barsch, R., Krischer, L., Megies, T., Behr, Y., Wassermann, J., 2010. ObsPy: A python toolbox for seismology. Seis. Res. Lett. 81, 530–533. http://dx.doi.org/10.1785/gssrl.81.3.530.
Birnie, C., Angus, D., Chambers, K., Stork, A.L., 2016. Analysis and models of pre-injection surface seismic array noise recorded at the Aquistore carbon storage site. Geophys. J. Int. 206, 1246–1260. http://dx.doi.org/10.1093/gji/ggw203.
Bourne, S., Crouch, S., Smith, M., 2014. A risk-based framework for measurement, monitoring and verification of the Quest CCS Project, Alberta, Canada. Int. J. Greenhouse Gas. Cont. 26, 109–126.
Castle, J.C., Creager, K.C., 1999. A steeply dipping discontinuity in the lower mantle beneath Izu-Bonin. J. Geophys. Res. 104, 7279–7292.
Chadwick, R.A., Noy, D.J., 2015. Underground CO_2 storage: demonstrating regulatory conformance by convergence of history-matched modeled and observed CO_2 plume behavior using Sleipner time-lapse seismics. Greenhouse Gas Sci. Technol. 5, 305–322.
Chambers, K., Kendall, J.-M., Brandsberg-Dahl, S., Rueda, J., 2010. Testing the ability of surface arrays to monitor microseismic activity. Geophys. Prospect. 58, 821–830.
Crone, A., Wheeler, R.L., 2000. Data for Quaternary Faults, Liquefaction Features, and Possible Tectonic Features in the Central and Eastern United States, East of the Rocky Mountain Front, Open-File Report 00-260. U.S. Geological Survey.
Drew, J., Leslie, D., Armstrong, P., Michaud, G., 2005. Automated microseismic event detection and location by continuous spatial mapping. In: SPE-95513 SPE Annual Technical Conference and Exhibition. Dallas, Texas.
Earle, P.S., Shearer, P.M., 1994. Characterization of global seismograms using an automatic-picking algorithm. Bull. Seis. Soc. Am. 84, 366–376.
Eisner, L., Duncan, P.M., Heigl, W.M., Keller, W.R., 2009. Uncertainties in passive seismic monitoring. Lead. Edge 28, 648–655.
Evans, J.R., Allen, S.S., 1983. A teleseism-specific detection algorithm for single short-period traces. Bull. Seis. Soc. Am. 73, 1173–1186.
Evans, W.M., 1973. A System for Combined Determination of Dynamic and Static Properties, Permeability, Porosity, and Resistivity of Rocks. UT, Austin (Ph.D. thesis).
Finley, R.J., Frailey, S.M., Leetaru, H.E., Senel, O., Coueslan, M.L., Marsteller, S., 2013. Early operational experience at a one-million Tonne CCS demonstration project, Decatur, Illinois, USA. Energy Procedia 37, 6149–6155. http://dx.doi.org/10.1016/j.egypro.2013.06.544.
Frohlich, C., Walter, J.I., Gale, J.F.W., 2015. Analysis of transportable array (USArray) data shows earthquakes are scarce near injection wells in the Williston Basin, 2008–2011. Seis. Res. Lett. 86, 492–499.
Gaucher, E., 2015. Earthquake detection probability within a seismically quiet area: application to the Bruchsal geothermal field. Geophys. Prospect. 64, 268–286. http://dx.doi.org/10.1111/1365-2478.12270.
Gendzwill, D.J., Horner, R.B., Hasegawa, H.S., 1982. Induced earthquakes at a potash mine near Saskatoon, Canada. Can. J. Earth Sci. 19, 466–475.
Gibbons, S.J., Ringdal, F., 2006. The detection of low magnitude seismic events using array-based waveform correlation. Geophys. J. Int. 165, 149–166. http://dx.doi.org/10.1111/gji.2006.165.issue-1.
Goertz-Allmann, B.P., Gibbons, S.J., Oye, V., Bauer, R., Will, R., 2017. Characterization of induced seismicity patterns derived from internal structure in event clusters. J. Geophys. Res. 122, 3875–3894. http://dx.doi.org/10.1002/2016JB013731.
Haimson, B., Fairhurst, C., 1969. Hydraulic fracturing in porous-permeable materials. J. Pet. Technol. 21http://dx.doi.org/10.2118/2354-PA. SPE-2354-PA.
Harris, K., White, D., Melanson, D., Samson, C., Daley, T.M., 2016. Feasibility of time-lapse VSP monitoring at the Aquistore CO_2 storage site using a distributed acoustic sensing system. Int. J. Greenhouse Gas Cont. 50, 248–260. http://dx.doi.org/10.1016/j.ijggc.2016.04.016.
Hawkes, C.D., Gardner, C., 2012. Wellbore integrity. In: Hitchon, B. (Ed.), Best Practices for Validating CO2 Geological Storage: Observations and Guidance from the IEAGHG Weyburn-Midale CO2 Monitoring and Storage Project. Geoscience Publishing, Edmonton, pp. 255–288.
Heidbach, O., Tingay, M., Barth, A., Reinecker, J., Kurfeß, D., Müller, B., 2010. Global crustal stress pattern based on the World Stress Map database release 2008. Tectonophysic 482, 3–15.
Hlidek, B.T., Rieb, B., 2011. Fracture stimulation treatment best practices in the Bakken oil shale. SPE 140252. In: SPE Hydraulic Fracturing Technology Conference and Exhibition. Woodlands, TX. (10 p).
Horner, R.B., Hasegawa, H.S., 1978. Seismotectonics of Southern Saskatchewan. Canadian J. Earth Sci. 15, 1341–1355.
Hubbert, M.K., Rubey, W.W., 1959. Role of fluid pressure in mechanics of overthrust faulting. Geol. Soc. Am. Bull. 70, 115–206. http://dx.doi.org/10.1130/0016-7606(1959)70[115:ROFPIM]2.0.CO;2.
IEAGHGS, 2014. CO_2 Storage Efficiency in Deep Saline Formations: A Comparison of Volumetric and Resource Estimation Methods, Report 2014/09.
Inbal, A., Clayton, R.W., Ampuero, J.-P., 2015. Imaging widespread seismicity at mid-lower crustal depths beneath Long Beach, CA, with a dense seismic array: evidence for a depth-dependent earthquake size distribution. Geophys. Res. Lett. 42, 6314–6323. http://dx.doi.org/10.1002/2015GL064942.
Jahan, I., Castagna, J., Murphy, M., 2017. Fault detection from 3-D seismic data and distribution of conjugate faults in the Bakken formation. In: Unconventional Resources Technology Conference. Austin, Texas, 24–26 July 2017. pp. 385–393.
Jiang, T., Pekot, L.J., Jin, L., Peck, W.D., Gorecki, C.D., Worth, K., 2017. Numerical modelling of the Aquistore CO_2 storage project. Energy Procedia 114, 4886–4895. http://dx.doi.org/10.1016/j.egypro.2017.03.1630.
Kaven, J.O., Hickman, S.H., McGarr, A.F., Ellsworth, W.L., 2015. Surface monitoring of microseismicity at the Decatur, Illinois, CO_2 sequestration demonstration site. Seis. Res. Lett. 86, 1–6. http://dx.doi.org/10.1785/0220150062.
Kennett, B.L.N., 2000. Stacking three-component seismograms. Geophys. J. Int 141, 263–269.
Kent, D.M., Christopher, J.E., 1994. Geological history of the Williston Basin and the Sweetgrass Arch. In: Mossop, G., Shetsen, I. (Eds.), Geological Atlas of the Western Canada Sedimentary Basin. Canadian Society of Petroleum Geologists and Alberta Research Council, Calgary and Edmonton, pp. 421–429.
Kim, W.-Y., 2013. Induced seismicity associated with fluid injection into a deep well in Youngstown, Ohio. J. Geophys. Res. 118, 3506–3518. http://dx.doi.org/10.1002/jgrb.50247.
Kreis, L.K., Ashton, K.E., Maxeiner, R.O., 2000. Geology of the Precambrian basement and Phanerozoic strata in Saskatchewan, Sheet 1 of 8, Lower Paleozoic map series, Saskatchewan Energy Mines. Open File Rep. 2000–2002.
Larsen, S., Grieger, J., 1998. Elastic modeling initiative, Part III: 3-D computational modeling. SEG Expand. Abstr. 68, 1803–1806.
Li, X., Shang, X., Wang, Z., Dong, L., Weng, L., 2016. Identifying P-phase arrivals with noise: an improved Kurtosis method based on DWT and STA/LTA, J. App. Geophys 133, 50–61.
Lomax, A., Virieux, J., Volant, P., Berge, C., 2000. Probabilistic earthquake location in 3D and layered models: introduction of a Metropolis-Gibbs method and comparison with linear locations. In: Thurber, C.H., Rabinowitz, N. (Eds.), Advances in Seismic Event Location. Kluwer Amsterdam, pp. 101–134.
Lomax, A., Zollo, A., Capuano, P., Virieux, J., 2001. Precise absoute earthquake location under Somma-Vesuvius volcano using a new 3D velocity model. Geophys. J. Int. 146, 313–331.

MacBeth, C., 2002. Multi-Component VSP Analysis for Applied Seismic Anisotropy. Oxford, United Kingdom, United Kingdom, Pergamon.
Maxwell, S., 2010. Microseismic: growth born from success. Lead. Edge 29, 338–343.
McGarr, A., Simpson, D., Seeber, L., 2002. Case histories of induced and triggered seismicity. International Handbook of Earthquake and Engineering Seismology, vol. 8 Academic Press Waltham, MA (chap. 40).
McLennan, J.D., Hasegawa, H.S., Roegiers, J.-C., Jessop, A., 1986. Hydraulic fracturing experiment at the University of Regina campus. Can. Geotech. J. 23, 548–555.
McNutt, S.R., 1986. Observations and analysis of B-type earthquakes explosions, and volcanic tremor at Pavlof Volcano, Alaska. Bull. Seis. Soc. Am. 76, 153–175.
Melendez-Martinez, J., Schmitt, D.R., 2016. A comparative study of the anisotropic dynamic and static elastic moduli of unconventional reservoir shales: implications for geomechanical investigations. Geophysics 81, D245–D261.
Mohan, G., Rai, S.S., 1992. Imaging of seismic scatterers beneath the Gauribidanur (GBA) array. Phys. Earth and Plan. Int. 71, 36–45.
Muirhead, K.J., Datt, R., 1976. The *N*-th root process applied to seismic array data. Geophys. J. R. Astron. Soc. 47, 197–210.
Nixon, C.G., Schmitt, D.R., Kofman, R.S., White, D., Stork, A., Kendall, M., Worth, K., 2017. Experiences in Deep Downhole Digital Microseismic Monitoring near 3 km at the PTRC Aquistore CO2 Sequestration Project. Geoconvention, Calgary.
Nuttli, O.W., 1973. Seismic wave attenuation and magnitude relations for Eastern North America. J. Geophys. Res. 78, 876–885.
O'Brien, S., Rock, L., 2016. Quest – Year 1 of commercial operations. In: IEAGHG Monitoring and Modelling Networks Meeting. Edinburgh.
Ong, O.N., Schmitt, D.R., Kofman, R.S., Haug, K., 2016. Static and dynamic pressure sensitivity anisotropy of a calcareous shale. Geophys. Prosp. 64, 875–897.
Oropeza Bacci, V., O'Brien, S., Anderson, M., Dahlby, K., Henderson, N., 2017. Microseismic monitoring results from CO2 storage operations at Quest. EAGE/SEG Research Workshop 2017. Trondheim, Expanded Abstract. https://doi.org/10.3997/2214-4609.201701959.
Pekot, L., 2016. An Update of Aquistore's CO_2 Storage Simulation. Aquistore AGM (16 August 2016).
Reiter, K., Heidbach, O., Schmitt, D., Haug, K., Ziegler, M., Moeck, I., 2014. A revised crustal stress orientation database for Canada. Tectonophys 636, 111–124.
Ringrose, P.S., Mathieson, A.S., Wright, I.W., Selama, F., Hansen, O., Bissell, R., Saoula, N., Midgley, J., 2013. The In Salah CO2 storage project: lessons learned and knowledge transfer. Energy Proc. 37, 6226–6236.
Roach, L.A.N., White, D.J., Roberts, B., 2015. Assessment of 4D seismic repeatability and CO_2 detection limits at the Aquistore CO_2 Storage Site. Geophys. 80, WA1–WA13. http://dx.doi.org/10.1190/GEO2014-0201.1.
Roach, L.A.N., White, D.J., Roberts, B., Angus, D., 2017. Initial 4D seismic results after CO2 injection start-up at the Aquistore storage site. Geophysic 82, B95–B107. http://dx.doi.org/10.1190/geo2016-0488.1.
Ross, J., Parrott, K., Vermilye, J., Klaus, A., 2017. Tomographic fracture imaging: examples of induced fracture and reservoir-scale observations during wellbore stimulations, Niobrara and Bakken plays, USA. Lead. Edge 36, 437–444. http://dx.doi.org/10.1190/tle36050437.1.
Rost, S., Thomas, C., 2002. Improving seismic resolution through array processing techniques. Surv. Geophys. 30, 271–299. http://dx.doi.org/10.1007/s10712-009-9070-6.
Rost, S., Thomas, C., 2009. Array seismology: methods and applications. Rev. Geophys. 40 (3). http://dx.doi.org/10.1029/2000RG000100.
Rostron, B., White, D., Hawkes, C., Chalaturnyk, R., 2014. Characterization of the Aquistore CO2 Project storage site, Saskatchewan, Canada. Energy Proc. 63, 2977–2984. http://dx.doi.org/10.1016/j.egypro.2014.11.320.
Sambridge, M., 1999. Geophysical inversion with a neighbourhood algorithm – I. searching a parameter space. Geophys. J. Int. 138, 479–494.
Saragiotis, C.D., Hadjileontiadis, L.J., Panas, S.M., 2002. PAI-S/K: a robust automatic seismic P phase arrival identification scheme. IEEE Trans. Geosci. Remote Sens. 40, 1395–1404.
Schmitt, D.R., Currie, C.A., Zhang, L., 2012. Crustal stress determination from boreholes and rock cores: fundamental principles. Tectonophys 580, 1–26.
Schmitt, D.R., 2014. Basic geomechanics for induced seismicity: a tutorial. Can. Soc. Explor. Geophys. Rec. 40, 24–29.
Skoumal, R.J., Brudzinski, M.R., Currie, B.S., Levy, J., 2014. Optimizing multi-station earthquake template matching through re-examination of the Youngstown, Ohio, sequence. Earth Planet. Sci. Lett. 405, 274–280.
Skoumal, R.J., Brudzinski, M.R., B. Currie, S., 2016. An efficient repeating signal detector to investigate earthquake swarms. J. Geophys. Res. Solid Earth 121, 5880–5897. http://dx.doi.org/10.1002/2016JB012981.
Sleeman, R., van Eck, T., 1999. Robust automatic P-phase picking: an on-line implementation in the analysis of broadband seismogram recordings. Phys. Earth Planet. Int. 113, 265–275. http://dx.doi.org/10.1016/S0031-9201(99)00007-2.
Stork, A.L., Verdon, J.P., Kendall, J.-M., 2015. The microseismic response at the In Salah carbon capture and storage (CCS) site. Int. J. Greenhouse Gas Cont. 32, 159–171.
Tarantola, A., Valette, B., 1982. Inverse problems = quest for information. J. Geophys. 50, 159–170.
Thomas, G.E., 1974. Lineament block tectonics – Williston-Blood Creek basin. AAPG Bull.-Am. Assoc. Petrol. Geol. 58, 1305–1322.
Tucker, O., Gray, L., Maas, W., O'Brien, S., 2016. Quest commercial scale CCS – the first year, IPTC-18666. In: International Petroleum Technology Conference. Bangkok.
Turino, C., Scafidi, D., Eva, E., Solarino, S., 2009. Inferences on active faults at the Southern Alps–Liguria basin junction from accurate analysis of low energy seismicity. Tectonophys 475, 470–479.
Verdon, J.P., Kendall, J.-M., White, D.J., 2012. Monitoring carbon dioxide storage using passive seismic techniques. Energy 165, 85–96.
Verdon, J.P., Kendall, J.-M., Horleston, A.C., Stork, A.L., 2016. Subsurface fluid injection and induced seismicity in southeast Saskatchewan. Int. J. Greenhouse Gas Cont. 54, 429–440. http://dx.doi.org/10.1016/j.ijggc.2016.04.007.
Verdon, J.P., Kendall, J.-M., Jicks, S.P., Hill, P., 2017. Using beamforming to maximise the detection capability of small, sparse seismometer arrays deployed to monitor oil field activities. Geophys. Prosp. 65, 1582–1596. http://dx.doi.org/10.1111/1365-2478.12498.
Verdon, J.P., 2014. Significance for secure CO_2 storage of earthquakes induced by fluid injection. Environ. Res. Lett. 9. http://dx.doi.org/10.1088/1748-9326/9/6/064022.
Warpinski, N.R., 1989. Viscoelastic constitutive model for determining in-situ stress magnitudes from anelastic strain recovery of core. SPE Prod. Eng. 4, 272–280.
White, D.J., Thomas, M.D., Jones, A.G., Hope, J., Nemeth, B., Hajnal, Z., 2005. Geophysical transect across a Paleoproterozoic continent–continent collision zone: the trans-Hudson Orogen. Can. J. Earth Sci. 42, 385–402.
White, D.J., Hawkes, C.D., Rostron, B.J., 2016. Geological characterization of the Aquistore CO2 storage site from 3D seismic data. Int. J. Greenhouse Gas Cont. 54, 330–344. http://dx.doi.org/10.1016/j.ijggc.2016.10.001.
White, D., Harris, K., Roach, L., Roberts, B., Worth, K., Stork, A., Nixon, C., Schmitt, D., Daley, T., Samson, C., 2017. Monitoring results after 36 ktonnes of deep CO2 injection at the Aquistore CO2 storage site Saskatchewan, Canada. Energy Proc. 114, 4056–4061.
Will, R., El-Kaseeh, G., Jaques, P., Carney, M., Greenberg, S., Finley, R., 2016. Microseismic data acquisition, processing, and event characterization at the Illinois Basin – Decatur Project. Int. J. Greenhouse Gas Cont. 54, 404–420. http://dx.doi.org/10.1016/j.ijggc.2016.01.007.
Wilson, M., Monea, M., 2004. IEA GHG Weyburn CO2 monitoring and storage project summary report 2000-$_2$ monitoring and storage project summary report 2000–2004. In: Wilson, M., Monea, M. (Eds.), From the Proceedings of the 7th International Conference on Greenhouse Gas Control Technologies. Petroleum Technology Research Centre, Regina.
Withers, M., Aster, R., Young, C., Beiriger, J., Harris, M., Moore, S., Trujillo, J., 1998. A comparison of select trigger algorithms for automated global seismic phase and event detection. Bull. Seis. Soc. Am. 88, 95–106.
Worth, K., White, D., Chalaturnyk, R., Sorensen, J., Hawkes, C., Rostron, B., Johnson, J., Young, A., 2014. Aquistore Project measurement, monitoring and verification: from concept to CO2 injection. Energy Procedia 63, 3202–3208. http://dx.doi.org/10.1016/j.egypro.2014.11.345.
Yoon, C.E., O'Reilly, O., Bergen, K.J., Beroza, G.C., 2015. Earthquake detection through computationally efficient similarity search. Sci. Adv. 1, e1501057.
Zoback, M.D., 2007. Reservoir Geomechanics. Cambridge University Press, Cambridge. http://dx.doi.org/10.1017/CBO9780511586477.